Cell Reports

Article

Fibroblast MrgprX2/B2 signaling drives hypertrophic scar fibrosis

Graphical abstract

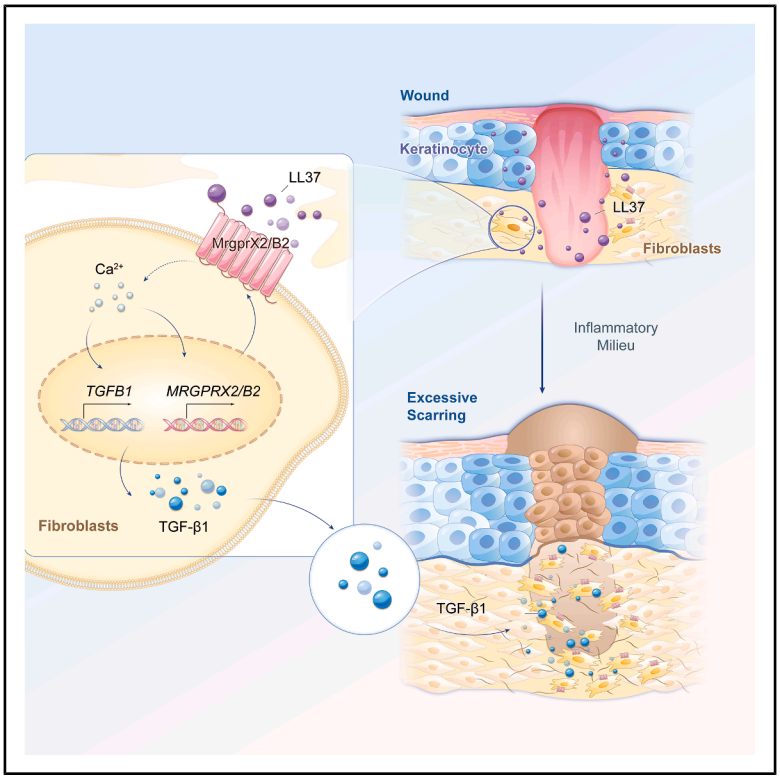

Authors

Heng Xu, Meiying Sheng, Yuxin Jia, ..., Yan Liu, Jing Feng, Yixin Zhang

Correspondence

xuh1990@gmail.com (H.X.), fengjing@simm.ac.cn (J.F.), zhangyixin6688@hotmail.com (Y.Z.)

In brief

Xu et al. identify MrgprX2/B2 as an inducible pro-fibrotic receptor in dermal fibroblasts. Activated by LL37, this receptor triggers a calcium-dependent signaling axis that promotes TGF-β1 production and myofibroblast transformation. These findings position MrgprX2/B2 as a promising therapeutic target for hypertrophic scarring.

Highlights

- MrgprX2/B2 is upregulated in dermal fibroblasts in hypertrophic scar tissue
- LL37 activates fibroblast MrgprX2/B2, triggering TGF-β1 release and proliferation
- MrgprX2/B2-mediated calcium signaling drives pathological fibrotic remodeling
- Genetic ablation of fibroblast MrgprB2 alleviates skin fibrosis *in vivo*

Xu et al., 2026, Cell Reports *45*, 117616
July 28, 2026
https://doi.org/10.1016/j.celrep.2026.117616

CellPress

Cell Reports

CellPress
OPEN ACCESS

Article

Fibroblast MrgprX2/B2 signaling drives hypertrophic scar fibrosis

Heng Xu,[1,8,9,10,*] Meiying Sheng,[1,9] Yuxin Jia,[1,2,9] Yi Luo,[1] Liyan Wu,[3] Luxian Zhou,[4] Zihan Wang,[3] Jiawei Sun,[5] Tianyi Shen,[3] Liqin Zhou,[3] Ting Wang,[3] Yan Liu,[6] Jing Feng,[3,7,*] and Yixin Zhang[1,*]

[1]Department of Plastic and Reconstructive Surgery, Shanghai Ninth People's Hospital, Shanghai Jiao Tong University School of Medicine, Shanghai 200011, China
[2]Department of Burn and Plastic Surgery, Beijing Children's Hospital, Capital Medical University, Beijing 100000, China
[3]State Key Laboratory of Chemical Biology, Shanghai Institute of Materia Medica, Shanghai 201203, China
[4]Research Center, Shanghai Archgene Biotechnology Co., Ltd, Shanghai 200011, China
[5]Genekinder Medicaltech (Shanghai) Co., Ltd, Shanghai 200011, China
[6]Department of Burn and Plastic Surgery, Ruijin Hospital, Shanghai Jiao Tong University School of Medicine, Shanghai 200011, China
[7]University of Chinese Academy of Sciences, Beijing 100000, China
[8]Shanghai Key Laboratory of Tissue Engineering, Shanghai Ninth People's Hospital, Shanghai Jiao Tong University School of Medicine, Shanghai 200011, China
[9]These authors contributed equally
[10]Lead contact
*Correspondence: xuh1990@gmail.com (H.X.), fengjing@simm.ac.cn (J.F.), zhangyixin6688@hotmail.com (Y.Z.)
https://doi.org/10.1016/j.celrep.2026.117616

SUMMARY

Hypertrophic scarring (HTS) represents a common clinical challenge characterized by excessive fibroblast activation and tissue fibrosis. However, the upstream signals driving pathological fibroblast proliferation remain poorly understood. Here, we identify the G protein-coupled receptor MrgprX2 (human)/MrgprB2 (mouse), traditionally restricted to mast cells, as an inducible pro-fibrotic receptor in dermal fibroblasts during HTS progression. MrgprX2 is markedly upregulated in dermal fibroblasts from HTS, and pharmacological inhibition of MrgprX2 significantly reduces fibrosis in humanized skin organoid models. In mouse studies, the endogenous peptide LL37 emerged as an MrgprX2/B2 activator in fibroblasts, triggering calcium influx, transforming growth factor β1 (TGF-β1) secretion, and proliferation. Genetic ablation of MrgprB2 in fibroblasts significantly reduced fibrosis *in vivo*, establishing the LL37-MrgprX2/B2-TGF-β1 axis as a key mediator of fibroblast activation and fibrotic remodeling. Together, our findings position MrgprX2/B2 as a critical molecular link between tissue injury-associated signals and fibrotic pathology, offering a promising therapeutic target for fibroblast-driven fibrosis in HTS.

INTRODUCTION

Skin wound healing is a complex biological process involving the coordinated interaction of various cell types to restore tissue integrity.[1] However, in some individuals, this process results in abnormal scars, including hypertrophic scarring (HTS) and keloid lesions.[2] HTS is especially common, affecting 40%–70% of patients undergoing surgery and up to 94% of individuals recovering from burn injuries.[3] These scars have a profound impact on patients, causing pain, itching, restricted movement, and psychological distress due to their appearance.[4,5] Despite its high prevalence and significant impact on patients' quality of life, effective treatment options for HTS remain limited.

Fibroblasts are the principal mediators of skin fibrosis, playing a central role in extracellular matrix (ECM) deposition, tissue remodeling, and scar formation.[2,6,7] Under normal conditions, they help maintain skin homeostasis by producing structural components such as collagen, elastin, and proteoglycans.[8,9] During wound repair, however, fibroblasts undergo a prolonged phenotypic transformation into myofibroblasts, leading to tissue stiffening and excessive scarring.[10–12] Previous studies have identified several factors that contribute to fibroblast activation, including inflammatory signals, growth factors, and mechanical stress.[13,14] However, the mechanisms driving persistent fibroblast activation in skin fibrosis remain unclear. Recent advances establish the skin as a neuroimmuno-endocrine organ where keratinocytes, melanocytes, immune cells, and fibroblasts coordinately sense environmental stressors (trauma, antimicrobial peptides, UV radiation) and regulate local homeostasis.[15] Within this network, fibroblasts actively produce POMC-derived neuropeptides (e.g., α-MSH with antifibrotic effects), respond to CRH/urocortin signaling, and contribute to local glucocorticoid synthesis, yet how they directly detect injury-associated antimicrobial peptides remains unknown.

Mas-related G-protein-coupled receptor B2 (MrgprB2), the mouse ortholog of human MrgprX2, is predominantly expressed in connective tissue mast cells and mediates non-IgE-dependent activation in response to a variety of basic secretagogues, including neuropeptides, drugs, and antimicrobial peptides.[16–19]

MrgprX2/MrgprB2 plays a crucial role in neuroimmune interactions by promoting mast cell degranulation, leading to the release of pro-inflammatory mediators and the recruitment of immune cells to sites of tissue injury. This mechanism contributes to the pathogenesis of several conditions, including asthma, itch, neurogenic inflammation, and pain.[20–23] Emerging evidence indicates that MrgprX2/B2 expression can be dynamically upregulated during disease states, suggesting that its expression is modifiable by local inflammatory and tissue-specific signals.[12,24–26] These findings underscore the need for further exploration of the molecular pathways that drive disease progression through MrgprX2/B2 signaling.

With RNA-sequencing analysis of human HTS tissues, we revealed a significant upregulation of MrgprX2 expression in fibroblasts. Parallel to how environmental stressors reprogram resident cells to adopt neuroendocrine phenotypes,[15] LL37-induced MrgprX2/B2 expression transforms quiescent fibroblasts into pro-fibrotic effectors that sense injury signals normally restricted to mast cells. Complementary mechanistic studies using a modified mouse model of skin fibrosis demonstrated that MrgprB2 activation is critical for fibroblast-dependent release of transforming growth factor β1 (TGF-β1), which in turn promotes pathological fibrosis. These findings underscore the critical role of the MrgprX2/B2 signaling in promoting fibroblast activation and advancing fibrotic tissue remodeling.

RESULTS

MrgprX2 is functionally upregulated in fibroblasts within human hypertrophic scar tissue

To investigate the expression pattern of MrgprX2 in human skin fibrosis, we performed RNAscope fluorescent *in situ* hybridization. MrgprX2 mRNA was scarcely detectable in normal skin (NS) but was markedly upregulated in HTS tissues (Figure 1A). Although MrgprX2 has been traditionally considered mast cell-specific, only a minority of its signals overlapped with Avidin-positive mast cells, suggesting additional sources of expression. Noting that single-cell RNA-seq analysis revealed a significantly higher abundance of fibroblasts in HTS tissues compared to healthy skin (Figures 1B and 1C), we re-analyzed public protein expression datasets and found low but detectable levels of MrgprX2 in fibroblasts (Figure S1). These observations led us to hypothesize that fibroblasts may contribute to the elevated MrgprX2 expression in HTS.

To test this, we performed bulk RNA-sequencing on fibroblasts purified from NS and HTS tissues. Compared to NS fibroblasts, those from HTS displayed a clear activation profile. A heatmap of the top 20 upregulated genes included established fibroblast activation markers such as *GDF5* and *LRRC15*, consistent with fibrotic remodeling (Figures 1D and 1E). Among the Mrgpr gene family members (*MRGPR-X1*, *-X3*, *-X4*, *-D*, *-E*, *-F*, *-G*), only *MRGPRX2* was significantly upregulated in HTS fibroblasts (Figure 1F). Immunostaining confirmed that MrgprX2 signals primarily co-localized with α-SMA-positive fibroblasts, indicating its presence in activated fibroblast populations. These findings were corroborated by RT-qPCR and western blot analyses, which showed significantly higher *MRGPRX2* mRNA and protein levels in fibroblasts from HTS tissues (Figures 1G–1I).

To determine whether MrgprX2 was functionally expressed in fibroblasts, we cultured primary fibroblasts and performed calcium imaging in single living cells. Stimulation with the MrgprX2 agonist PAMP (9–20, also known as PAMP-12) showed that fibroblasts isolated from healthy skin displayed minimal $[Ca^{2+}]_i$ responses (Figure 1J). In contrast, approximately 80% of fibroblasts derived from HTS tissues exhibited robust calcium influx upon PAMP-12 stimulation (Figure 1K), significantly higher than the response observed in NS fibroblasts. Importantly, this response was abolished by small interfering RNA (siRNA)-mediated knockdown of *MRGPRX2* (Figures 1L–1M and S2), confirming that the observed calcium influx was specifically mediated through MrgprX2. To further characterize the hypertrophic phenotype of *MRGPRX2*-expressing fibroblasts, we assessed a broader panel of activation markers, including *MKI67*, *FAP*, *POSTN*, *COL1A1*, and *COL3A1* in addition to *ACTA2* and *COL1A2* (Figure S3). *MRGPRX2* siRNA knockdown significantly reduced the expression of all these downstream effectors. Notably, the expression of *LRRC15*, a top upregulated marker in the HTS fibroblast pool, remained unchanged following *MRGPRX2* ablation. This uncoupling indicates that *MRGPRX2* signaling does not strictly overlap with the entire *LRRC15*$^+$ lineage, but rather defines a distinct functional state driving the hyper-proliferative and pro-fibrotic phenotype within the activated fibroblast microenvironment.

Endogenous LL37 upregulates MrgprX2 to drive fibroblast activation and proliferation

Previous studies have shown that MrgprX2 can be activated by a variety of biologically active peptides. To identify an endogenous activator relevant to fibrotic conditions, we performed pan-tissue RNA-seq and found that *CAMP*, the gene encoding the antimicrobial peptide LL37, was significantly upregulated in HTS samples compared to healthy skin (Figure 2A). In contrast, other genes encoding endogenous secretagogues were either unchanged or are not known activators of MrgprX2. Supporting this transcriptomic evidence, immunofluorescence staining showed no detectable LL37 signal in healthy skin, whereas HTS tissues exhibited a pronounced LL37 signal, primarily localized in K14-positive keratinocytes (Figure 2B). This was further validated by RT-qPCR and western blotting, which confirmed elevated *CAMP* transcripts and increased protein levels of LL37 and its precursor hCAP18 in HTS tissues (Figures 2C, 2D, and S4).

To validate LL37 as a functional activator of MrgprX2, we performed calcium imaging in HFF1 cells engineered to overexpress MrgprX2. These cells showed robust intracellular calcium responses upon LL37 stimulation, in contrast to control cells (Figure S5). Consistent with this pattern, primary fibroblasts derived from healthy skin displayed minimal intracellular calcium responses to LL37 (Figure 2E), whereas fibroblasts from HTS tissues exhibited robust responses (Figure 2F). This response was effectively suppressed by siRNA knockdown of *MRGPRX2* or pharmacological blockade of MrgprX2 function (Figures 2G–2K), demonstrating that LL37 is a potent and specific upstream activator of MrgprX2 in the fibrotic microenvironment.

In addition to this direct activation, 24 h LL37 treatment significantly increased both the mRNA and protein levels of

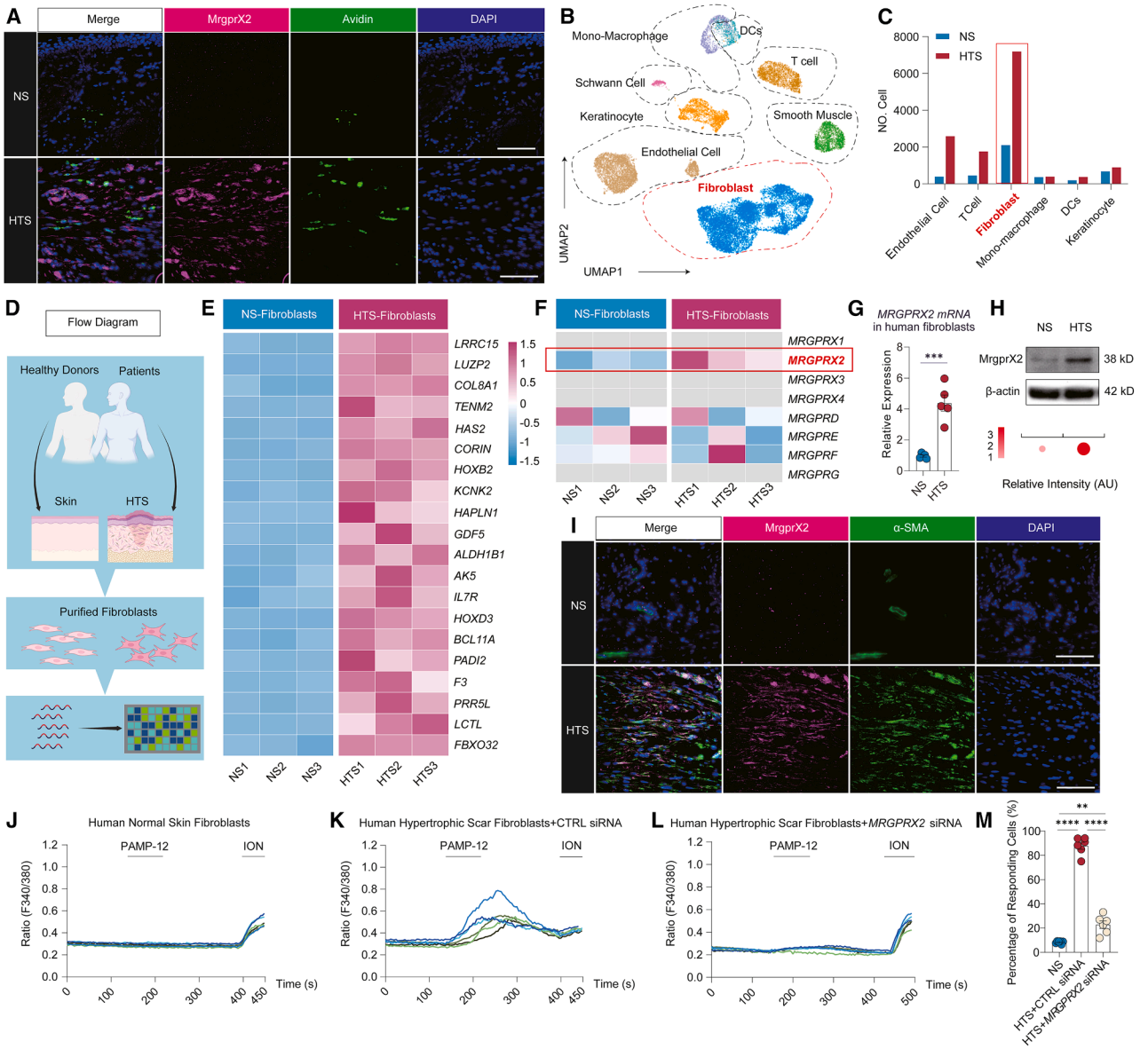

Figure 1. Fibroblasts upregulate MrgprX2 expression in hypertrophic scar lesions

(A) Representative images showing MrgprX2 expression in skin and hypertrophic scar tissues, co-stained with Avidin. n = 5 per group. Scale bars = 100 μm.

(B and C) scRNA-seq data showing (B) cell clustering and (C) increased fibroblast abundance in HTS versus NS.

(D) Schematic illustrating fibroblast isolation from NS and HTS tissues for bulk RNA-sequencing. Created with BioRender.com.

(E and F) Heatmaps of RNA-seq data from isolated fibroblasts (n = 3 per group), showing (E) the top 20 upregulated genes in HTS fibroblasts and (F) Mrgpr gene family expression profiles.

(G and H) RT-qPCR and western blot analysis confirming increased MrgprX2 expression in HTS fibroblasts (n = 3–5 per group). Student's t test.

(I) Immunostaining showing MrgprX2 expression co-localized with α-SMA$^+$ fibroblasts in NS and HTS tissues (n = 5 per group). Scale bars = 100 μm.

(J–M) Calcium imaging shows responses to PAMP-12 (50 nM) in (J) NS fibroblasts, (K) HTS fibroblasts, and (L) HTS fibroblasts after *MRGPRX2* knockdown, with (M) quantitative analysis (n = 6 cover slips per group). One-way ANOVA with Tukey's multiple comparison test. Data are shown as mean ± SEM. $^{**}p < 0.01$, $^{***}p < 0.001$, and $^{****}p < 0.0001$.

MrgprX2 in primary fibroblasts isolated from healthy skin (Figures 2L–2M), resulting in robust $[Ca^{2+}]_i$ responses compared with those in the vehicle-treated group (Figures 2N–2P). Moreover, LL37 treatment enhanced fibroblast viability compared to vehicle-treated controls, and this effect was significantly inhibited by *MRGPRX2* siRNA (Figures 2Q and 2R). These findings suggest that LL37 not only activates MrgprX2 signaling but also upregulates its expression, thereby contributing to fibroblast activation and proliferation in fibrotic skin.

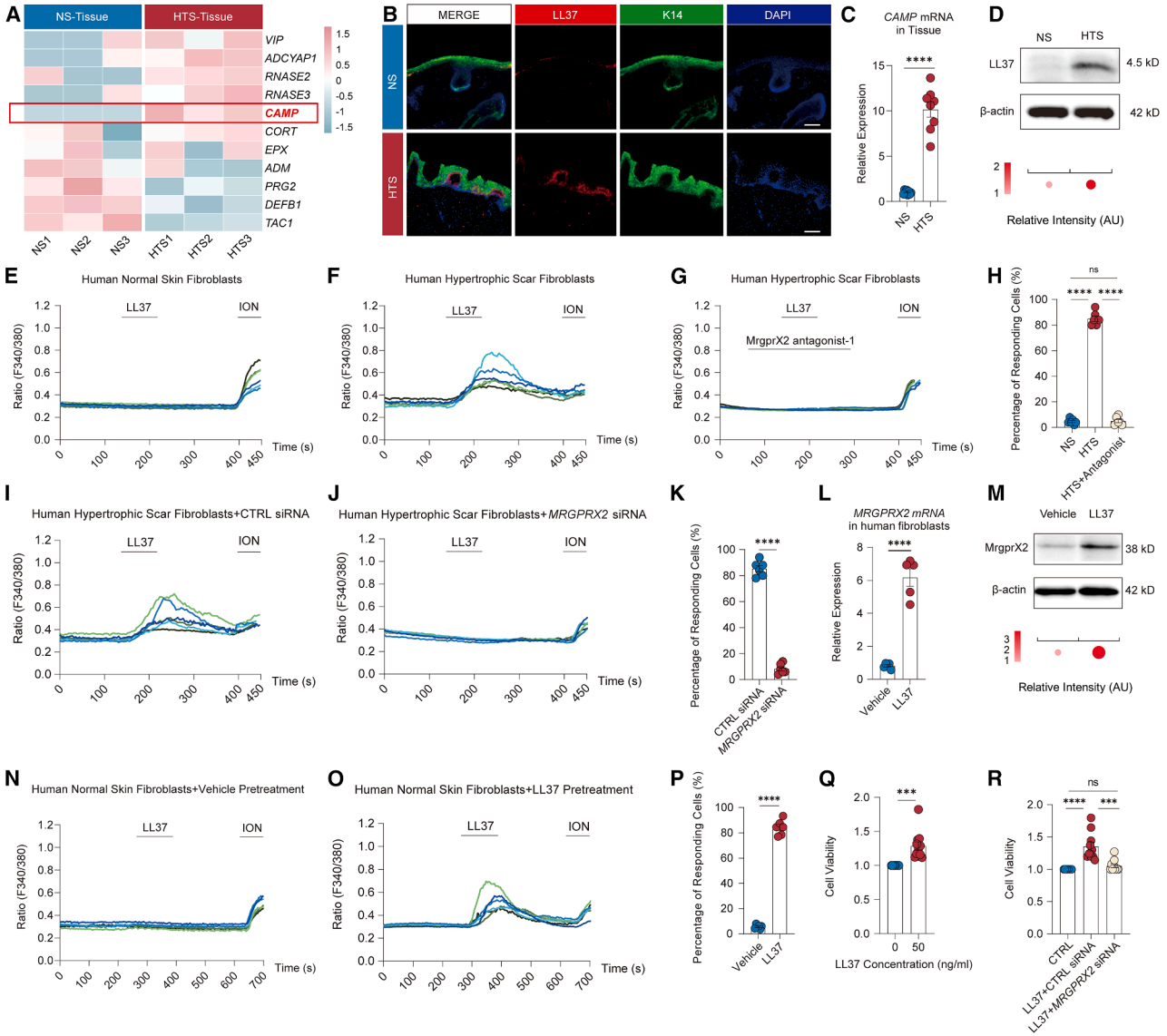

Figure 2. Endogenous LL37 upregulates MrgprX2 in fibroblasts in hypertrophic scar

(A) Heatmap from bulk RNA-seq analysis showing *CAMP* (LL37) upregulation in HTS tissues (n = 3 per group).

(B) Immunofluorescence of LL37 and K14 in NS and HTS tissues (n = 5 per group). Scale bars = 100 μm.

(C and D) RT-qPCR (n = 8 per group) and western blot (n = 3–5 per group) showing increased *CAMP* and LL37 levels in HTS fibroblasts. Student's t test.

(E–H) Calcium imaging of fibroblasts stimulated with LL37 (50 ng/mL): (E) NS, (F) HTS, (G) HTS pre-treated with MrgprX2 antagonist-1. (H) Quantification (n = 6 cover slips per group). One-way ANOVA with Tukey's multiple comparison test.

(I–K) Calcium imaging of HTS-derived fibroblasts stimulated with LL37 (50 ng/mL): (I) transfected with CTRL siRNA, (J) transfected with *MRGPRX2* siRNA. (K) Quantification (n = 6 cover slips per group). Student's t test.

(L and M) LL37-induced upregulation of MrgprX2 in fibroblasts derived from normal skin (NS), as shown by (L) RT-qPCR and (M) western blot. n = 3–5 per group. Student's t test.

(N–P) Calcium imaging of NS-derived fibroblasts pretreated with vehicle (N) or LL37 (O), and quantification (P). n = 6 cover slips per group. Student's t test.

(Q and R) CCK-8 assay showing LL37-induced fibroblast proliferation (Q), and the effect of *MRGPRX2* siRNA knockdown on LL37-induced proliferation (R) (n = 10 per group). Student's t test and One-way ANOVA with Tukey's multiple comparison test. Data are shown as mean ± SEM. ns: not significant. ***$p < 0.001$ and ****$p < 0.0001$.

LL37-MrgprX2 signaling in fibroblasts promotes fibrosis in a humanized skin organoid model

The reconstructed full-thickness 3D skin model, which contains both epidermis and dermis, has emerged as an innovative *in vitro* tool for investigating the complex processes of fibrotic progression, providing critical insights into the underlying molecular and cellular mechanisms of this pathology.[27] To generate this model, healthy donor-derived keratinocytes and fibroblasts were

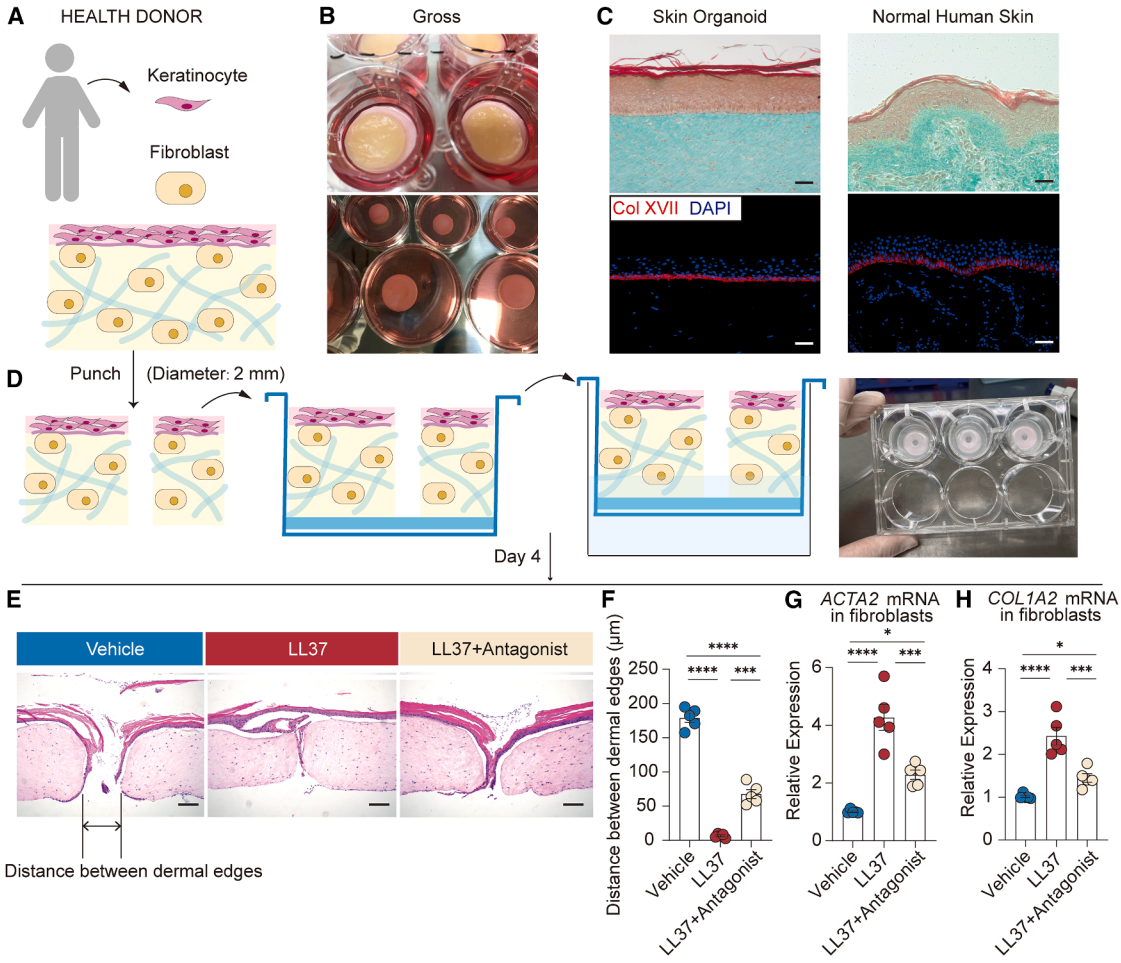

Figure 3. LL37 promotes fibroblast-driven fibrosis in a skin organoid model

(A) Diagram illustraes the construction of the humanized full-thickness skin organoid.

(B and C) Gross morphology (B) and Masson's trichrome and Collagen XVII staining (C) confirming epidermal and dermal structure ($n = 10$ per group). Scale bars = 100 μm.

(D) Schematic of full-thickness wound induction in the organoid.

(E) H&E staining shows wound morphology after 4 days of LL37 or LL37 + antagonist-1 treatment.

(F) Quantification of wound edge closure.

(G and H) RT-qPCR analysis of pro-fibrotic genes *ACTA2* and *COL1A2* ($n = 5$ per group). One-way ANOVA with Tukey's multiple comparison test. Data are shown as mean ± SEM. $^{*}p < 0.05$, $^{***}p < 0.001$, and $^{****}p < 0.0001$.

used to establish the humanized full-thickness 3D skin organoid (Figures 3A and 3B). Characterization with Masson's and Collagen XVII (pinpoint basement membrane) staining revealed that the organoids displayed epidermal and dermal layers closely resembling native skin morphology (Figure 3C). To simulate injury and evaluate fibrotic responses, full-thickness wounds were created in the skin organoids using a 1 mm biopsy punch (Figure 3D), and the organoids were cultured for four days under various treatment conditions. To thoroughly characterize the temporal impact of LL37, we performed a time-course analysis (day 0, day 1, day 4) on LL37-treated organoids using western blot for a comprehensive panel of pro-fibrotic and proliferative markers (Figure S6). This analysis revealed a significant and progressive upregulation of α-SMA, COL1A1, COL3A1, FAP, POSTN, and Ki67 protein levels from day 0 to day 4 in LL37-treated organoids, clearly indicating accelerated fibroblast activation, proliferation, and matrix deposition, consistent with fibrotic progression. While overt scarring was not apparent within this 4-day time frame, organoids treated with LL37 displayed accelerated wound closure and elevated expression of fibrotic markers compared to vehicle-treated controls (Figures 3E, 3F, and S6). In contrast, co-treatment with the MrgprX2 antagonist-1 significantly delayed wound healing and reduced expression of pro-fibrotic genes, including *ACTA2*, and *COL1A2* (Figures 3E–3H), highlighting the role of LL37-MrgprX2 signaling in promoting fibroblast-driven fibrosis.

LL37-induced mouse model recapitulates hypertrophic scarring

Clinical observations have identified a notable association between rosacea and HTS, and acute application of LL37 is known

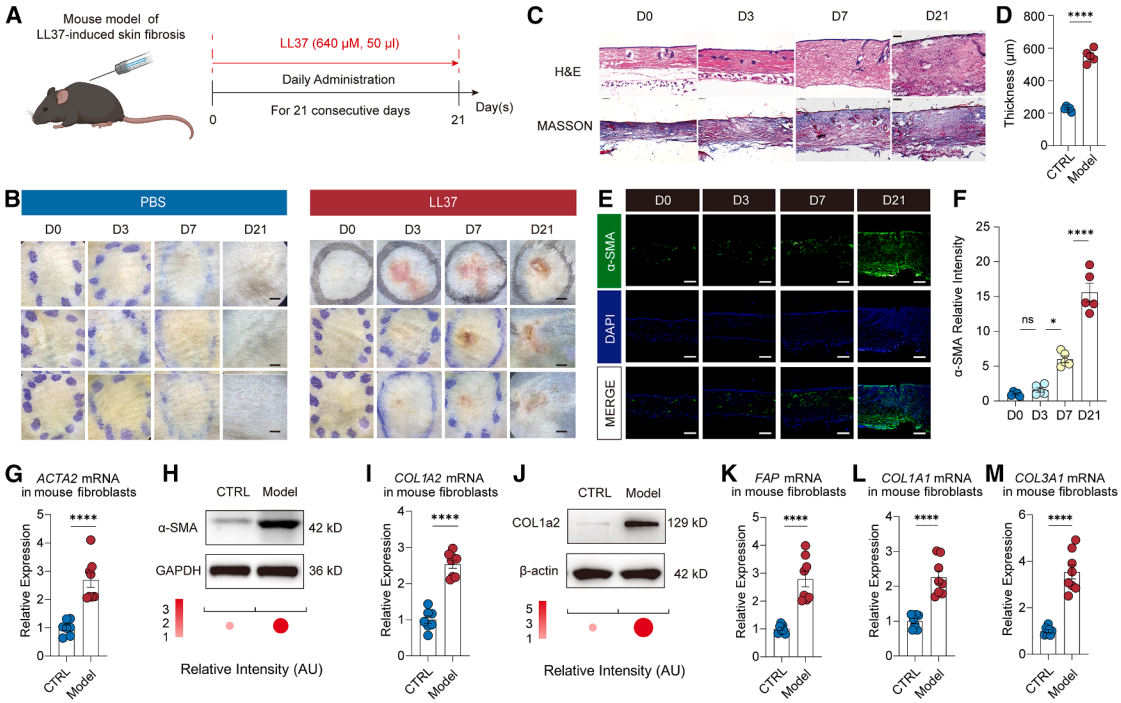

Figure 4. LL37 induces hypertrophic scar-like lesions in mice

(A) Diagram outlining the LL37-induced murine fibrosis model. Created with BioRender.com.

(B) Gross skin images over time following PBS or LL37 injection (n = 20 mice per group). Scale bars = 2.5 mm.

(C) H&E and Masson staining showing dermal thickening.

(D) Quantification of skin thickness (n = 5 per group). Scale bars = 100 μm. Student's t test.

(E and F) Representative images of α-SMA immunofluorescence and (F) quantification of fluorescence intensity (n = 5 per group). One-way ANOVA with Tukey's multiple comparison test.

(G–J) RT-qPCR and western blot showing elevated α-SMA and COL1a2 in fibroblasts (n = 3–8 per group). Student's t test.

(K–M) RT-qPCR analysis of *FAP*, *COL1A1*, and *COL3A1* expression in fibroblasts (n = 3–8 per group). Student's t test. Data are shown as mean ± SEM. ns: not significant. $^{*}p < 0.05$ and $^{****}p < 0.0001$.

to induce rosacea-like skin inflammation in mice.[28,29] Building on this, we adapted the LL37-induced rosacea-like model into a murine model of skin fibrosis by administering daily intradermal injections of 640 μM LL37 for 21 days (Figure 4A). By day 21, the wild-type (WT) mice exhibited skin lesions with hallmark features of fibrosis, including erythema, inelasticity, and rough, uneven skin texture (Figure 4B). Histological analysis revealed progressive dermal thickening, accumulation of α-SMA-positive fibroblasts, and the absence of skin appendages (Figures 4C–4F). Fibroblasts isolated from LL37-treated mice also showed upregulated expression of fibrosis-associated molecules, including α-SMA, COL1A2, *FAP*, *COL1A1,* and *COL3A1* (Figures 4G–4M), confirming LL37-induced myofibroblast activation. These findings demonstrate that our model effectively recapitulates key pathological features of human HTS.

Genetic ablation of MrgprB2 in fibroblasts alleviates skin fibrosis

We next examined the expression and functional significance of MrgprB2, the murine ortholog of human MrgprX2, in the LL37-induced fibrosis model. Consistent with the upregulation of MrgprX2 observed in human HTS tissues, MrgprB2 expression was significantly increased following LL37 treatment (Figure 5A). To assess the *in vivo* contribution of MrgprB2 to fibrosis, we subjected global *MRGPRB2* knockout (KO) mice and their WT littermates to the LL37-induced fibrosis model. Notably, compared to LL37-treated WT controls, *MRGPRB2* KO mice exhibited significantly attenuated fibrotic responses, including reduced lesion severity (Figure S7A), decreased skin thickness (Figures S7B and S7C), and diminished dermal fibrosis (Figures S7D and S7E). To identify the key cell types responsible for the fibrotic response, we crossed *MRGPRB2*^{cre} mice with tdTomato (*Ai9*) reporter mice (Figure 5B). Immunostaining revealed that, while a subset of MrgprB2 expression overlapped with Avidin-positive mast cells (Figure S8), the majority was localized to α-SMA-positive fibroblasts (Figure 5C). Consistent with this finding, mast cell-deficient *Kit*$^{w\text{-}sh}$ mice showed no significant improvement in fibrosis despite exhibiting markedly reduced infiltration of T cells, B cells, neutrophils, monocytes, and macrophages (Figures S9 and S10), suggesting that while mast cells regulate the immune microenvironment, LL37-driven fibrosis is primarily mediated through direct MrgprB2 signaling in fibroblasts. On the other hand, in fibroblasts isolated from LL37-treated mice, MrgprB2 expression was significantly elevated at both mRNA and protein levels (Figures 5D and 5E). *In vitro*, LL37 stimulation enhanced MrgprB2 expression and

CellPress
OPEN ACCESS

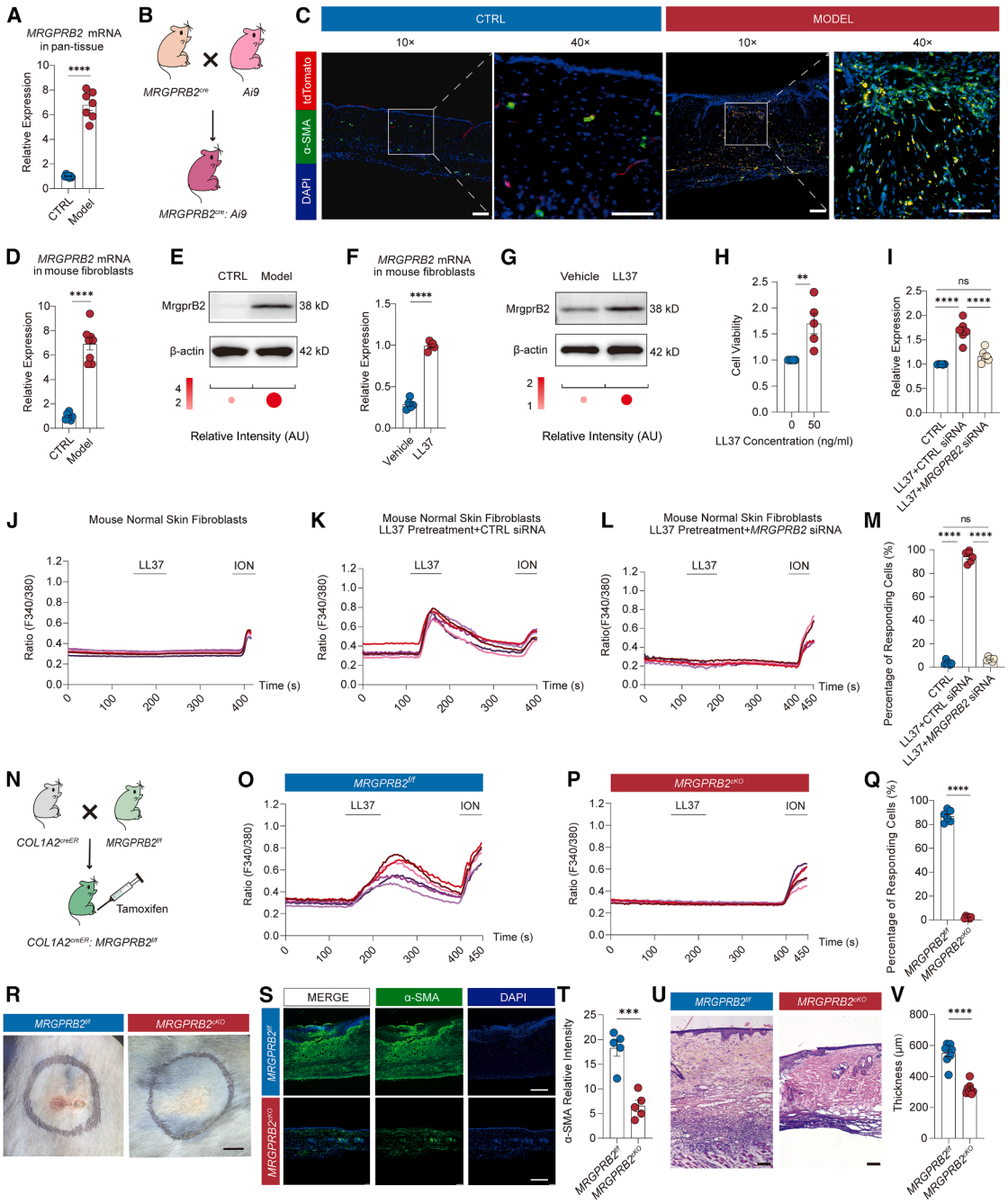

Figure 5. MrgprB2^{+} fibroblasts drive LL37-induced mouse skin fibrosis

(A) RT-qPCR of MrgprB2 expression in skin tissues (n = 7 per group).

(B and C) *MRGPRB2^{cre}; Ai9* reporter mice showing tdTomato^{+} fibroblasts co-localized with α-SMA (n = 5 per group). Scale bars, 250 μm (10×), 100 μm (40×).

(D–G) RT-qPCR and western blot analysis of MrgprB2 expression in lesion-derived and LL37-treated fibroblasts (n = 3–8 per group). Student's t test.

(H and I) CCK-8 assay showing increased fibroblast viability following LL37 treatment (H), and the effect of control siRNA or *MRGPRB2* siRNA on LL37-induced viability (I). n = 5 per group. Student's t test and One-way ANOVA with Tukey's multiple comparison test.

(J–M) Calcium imaging of mouse fibroblasts from vehicle-pretreated (J), LL37 pretreated cells transfected with CTRL siRNA, (J) LL37 pretreated cells transfected with *MRGPRB2* siRNA. (K) Quantification. n = 6 cover slips per group. One-way ANOVA with Tukey's multiple comparison test.

(N) Schematic of *COL1A2^{creER}: MRGPRB2$^{f/f}$* mouse generation.

(O–Q) Calcium imaging in fibroblasts from *MRGPRB2$^{f/f}$* (O) and *COL1A2^{creER}: MRGPRB2$^{f/f}$* (P) mice, with (Q) quantification (n = 6 cover slips per group). Student's t test.

(R–V) Gross skin images (R), α-SMA staining (S), fluorescence quantification (T), H&E staining (U), and lesion thickness (V) from the LL37-treated *MRGPRB2$^{f/f}$* and *COL1A2^{creER}: MRGPRB2$^{f/f}$* mice (n = 5–7 per group). Scale bars = 2.5 mm (R), 100 μm (S, U). Student's t test. Data are shown as mean ± SEM. ns: not significant. $^{**}p < 0.01$, $^{***}p < 0.001$, and $^{****}p < 0.0001$.

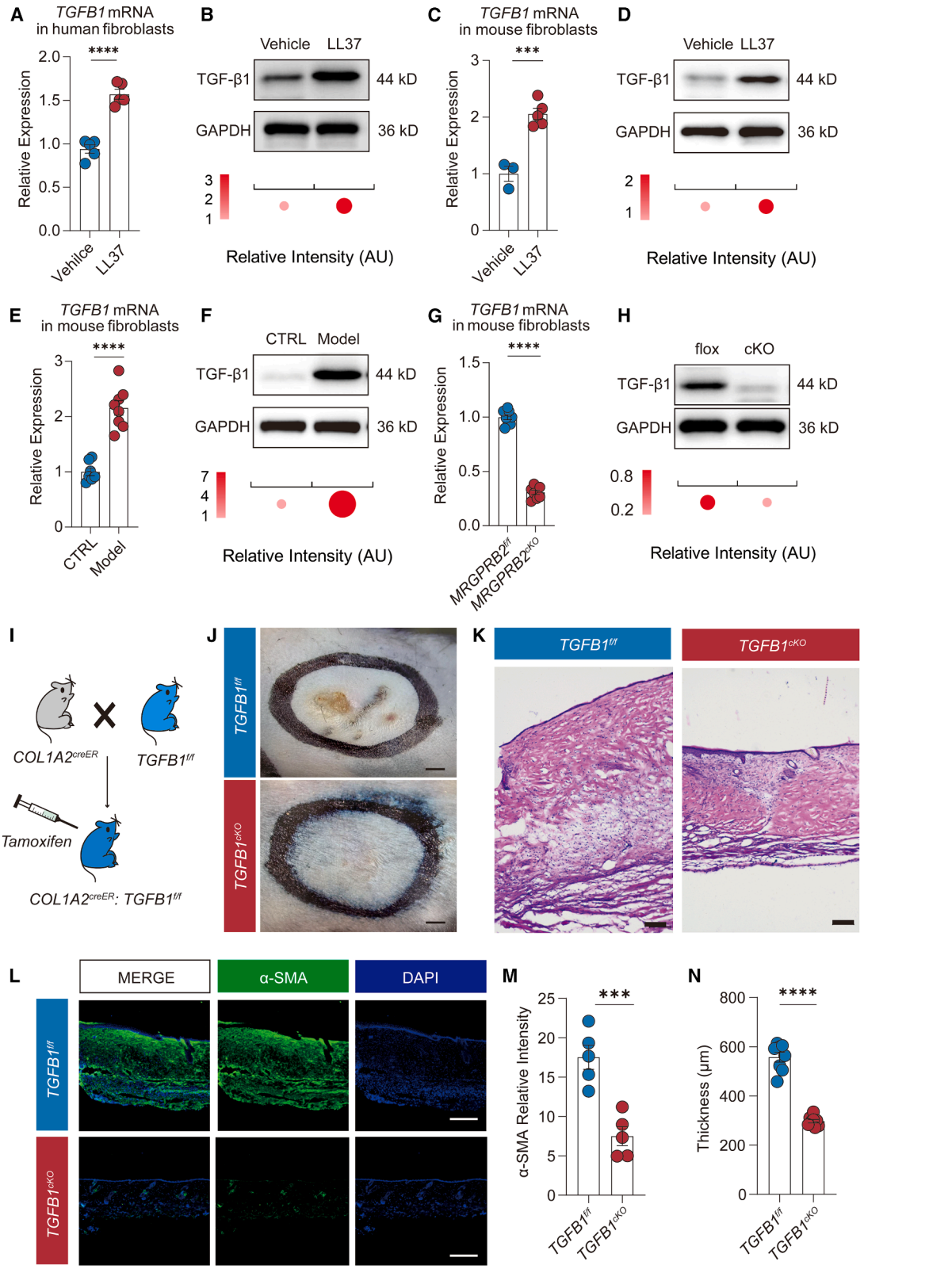

(legend on next page)

increased fibroblast viability (Figures 5F–5I; S11). Notably, nearly 90% of fibroblasts from LL37-treated mice exhibited calcium influx (Figures 5J and 5K), which was abolished by siRNA-mediated knockdown of *MRGPRB2* (Figures 5L–5M and S12), confirming its essential role in fibroblast activation.

To directly assess the role of fibroblast-expressed MrgprB2 in skin fibrosis, we generated the fibroblast-specific MrgprB2 KO mice by crossing *COL1A2*^{creER} with *MRGPRB2*$^{f/f}$ mice (Figure 5N). LL37 did not elicit any measurable $[Ca^{2+}]_i$ responses in the fibroblast isolated from LL37-treated *COL1A2*^{creER}*: MRGPRB2*$^{f/f}$ mice compared with that in the fibroblast isolated from LL37-treated *MRGPRB2*$^{f/f}$ mice (Figures 5O–5Q), indicating a reliable genetic ablation efficacy. Notably, following 21 days of LL37 treatment, *COL1A2*^{creER}*: MRGPRB2*$^{f/f}$ mice exhibited significantly milder erythema, smaller lesion sizes, markedly thinner tissue thickness, and a decreased density of α-SMA-positive fibroblasts compared to their littermate controls (*MRGPRB2*$^{f/f}$ mice) (Figures 5R–5V). These results demonstrate that fibroblast-expressed MrgprB2 is essential for promoting fibroblast activation and proliferation, and it contributes significantly to the development of skin fibrosis.

Downstream transforming growth factor β (TGF-β) signaling is crucial in tissue fibrosis

MrgprX2/B2-mediated calcium signaling plays a key role in regulating diverse biological processes.[30] To investigate its downstream effects, we re-analyzed RNA-sequencing data and found that genes associated with the Ca^{2+}/calmodulin-NFAT axis, such as *CALM1-3* and *NFACT1-2*, were significantly upregulated (Figures S13A and S13B), suggesting pathway activation (Figure S13C). Supporting this, RT-qPCR analysis revealed that fibroblasts from both human HTS tissues and LL37-induced fibrotic mouse models exhibited elevated expression of *PPP3CA* and *NFATC1*, *NFATC2,* compared to healthy controls (Figures S13D–S13I). Importantly, pharmacological inhibition of calcineurin with FK506 or blockade of NFAT with VIVIT significantly reversed this upregulation in cultured fibroblasts (Figures S13J–S13U), confirming the activation of the Ca^{2+}-calcineurin-NFAT signaling pathway. *In vivo*, *NFATC1* RNAscope staining confirmed that LL37-induced fibroblast NFAT activation is *MRGPRB2*-dependent and CsA-sensitive (Figure S14). Consequently, CsA treatment significantly attenuated dermal thickness in WT mice (Figure S15).

Given that the Ca^{2+}-Calcineurin-NFAT pathway is known to regulate the transcription of key fibrotic mediators, including TGF-β,[31–34] we next investigated how MrgprX2/B2 signaling influences TGF-β1 expression. Interestingly, TGF-β1 expression was markedly increased in LL37-treated fibroblasts derived from both human and mouse tissues (Figures 6A–6D), as well as in fibroblasts isolated from HTS-like lesions (Figures 6E and 6F). Notably, genetic ablation of *MRGPRB2* in fibroblasts significantly suppressed TGF-β1 expression (Figures 6G and 6H), further supporting that MrgprX2/B2-mediated calcium signaling acted as a critical upstream regulator of TGF-β1 transcription and drives fibrotic progression. To directly investigate the role of TGF-β1 in tissue fibrosis, we genetically ablated *TGFB1* in fibroblasts by crossing the *COL1A2*^{creER} with *TGFB1*$^{f/f}$ mice (Figure 6I). Following LL37-induced fibrosis, *COL1A2*^{creER}*: TGFB1*$^{f/f}$ mice exhibited milder erythema, smaller lesion sizes, reduced skin thickness, and decreased α-SMA intensity compared to their littermate controls (*TGFB1*$^{f/f}$ mice) (Figures 6J–6N). Together, these findings demonstrate that the Ca^{2+}-calcineurin-NFAT axis mediates TGF-β1 transcription via MrgprX2/B2-mediated calcium signaling, which plays a crucial role in driving tissue fibrosis. Beyond LL37, *MRGPRB2* deletion also impaired wound healing (Figure S16) and *MRGPRB2*$^{+}$ cells contributed to bleomycin-induced myofibroblast differentiation (Figure S17). While the initiating triggers differ across these models, the downstream consequence consistently converges on *MRGPRB2*-driven fibroblast activation, suggesting its role as a broader sensor in tissue repair and fibrosis.

DISCUSSION

The progression of fibrosis is strongly influenced by fibroblast interactions with immune cells through cell-cell communication.[35–38] While there is a low level of constitutive LL37 expression in most immune cells and epithelia, injury can significantly upregulate its expression in keratinocytes.[39–41] This raises the hypothesis that keratinocyte-fibroblast interactions may play a critical role in fibrosis through LL37-MrgprX2/B2-mediated reciprocal paracrine signaling. Such dynamic crosstalk may further create a feedback loop that sustains fibrotic processes, especially in pathological scar formation. Supporting this, sustained LL37 treatment in mice induced a HTS-like pathology, characterized by erythema, inelastic lesions, and increased dermal thickness. This mouse model provides a platform for investigating the molecular mechanisms driving skin fibrosis. Indeed, we found that fibroblast-expressed MrgprX2/MrgprB2 plays a detrimental role in skin fibrosis through downstream Ca^{2+}-dependent calcineurin-NFAT-TGF-β1 signaling, which is essential for fibroblast proliferation and myofibroblast transformation. Understanding the MrgprX2/MrgprB2-dependent acceleration of fibrotic processes via an autocrine mechanism may be critical for effectively mitigating excessive scarring. Importantly, the central role of calcium signaling in fibroblast activation must be considered alongside vitamin D signaling, a key regulator of calcium homeostasis, whose CYP11A1-derived metabolites

Figure 6. TGF-β1 mediates fibrosis downstream of fibroblast-expressed MrgprX2/B2 activation

(A–D) RT-qPCR and western blot analysis of TGF-β1 in LL37-treated primary human (A–B) and mouse (C–D) fibroblasts (n = 3–5 per group). Student's t test.

(E and F) TGF-β1 expression in fibroblasts from LL37-induced mouse fibrotic lesions (n = 3–8 per group). Student's t test.

(G and H) RT-qPCR and western blot analysis TGF-β1 expression in fibroblasts from *COL1A2*^{creER}*: MRGPRB2*$^{f/f}$ mice (n = 3–7 per group). Student's t test.

(I) Diagram of the generation of *COL1A2*^{creER}*; TGFB1*$^{f/f}$ mice.

(J–N) Gross skin images (J), H&E staining (K), α-SMA staining (L), fluorescence quantification (M), and lesion thickness (N) from the LL37-treated *TGFB1*$^{f/f}$ and *COL1A2*^{creER}*: TGFB1*$^{f/f}$ mice (n = 5–7 per group). Scale bars, 2.5 mm (J), 100 μm (K–L). Student's t test. Data are shown as mean ± SEM. ***$p < 0.001$ and ****$p < 0.0001$.

exhibit potent anti-fibrotic activities by suppressing TGF-β1-induced collagen deposition.[42] This interplay suggests that therapeutic strategies targeting MrgprX2/B2 may benefit from concurrent modulation of the vitamin D pathway to counteract pathological fibrosis.

MrgprX2/MrgprB2 has traditionally been considered a mast cell-specific marker, primarily expressed in connective tissue-type mast cells rather than mucosal mast cells.[12,43] Notably, the engraftment of human hematopoietic stem cells into humanized mice resulted in MrgprX2 expression exclusively in skin-engrafted connective tissue mast cells,[44] suggesting that connective tissue-specific signals are essential for sustaining MrgprX2 expression and function in preserving tissue integrity and mediating response to injury. Given that fibroblasts are the predominant cell type in connective tissue and play a central role in maintaining the structural and functional tissue integrity by producing ECM components, cytokines, and growth factors,[45] it is plausible to hypothesize that MrgprX2 expression may vary along a spectrum of resident cell activation states, depending on local tissue signals and inflammatory cues. Specific connective tissue-derived factors may promote the upregulation of this receptor in mast cells and even other cell types.

Interestingly, recent studies indicate that MrgprX2 expression is dynamically regulated in response to inflammatory stimuli, infections, or drug exposure, suggesting that its upregulation may be context- or disease-state-dependent.[25,46–48] Beyond mast cells, MrgprX2 has also been detected on other immune cells, such as basophils and eosinophils, albeit at lower levels and typically under specific conditions, with expression increasing in response to environmental stimuli.[49] These findings are consistent with our sequencing data, showing that while quiescent fibroblasts exhibit negligible MrgprX2/MrgprB2 expression, this GPCR is significantly upregulated under pathological conditions and mediates calcium influx upon LL37 stimulation. These dynamic changes suggest that MrgprX2 contributes to disease progression when ectopically expressed in non-canonical cell types such as fibroblasts. While our data identify *MRGPRX2* as a critical functional driver of fibroblast activation, the precise overlap of this *MRGPRX2*$^{+}$ state with established fibroblast subsets (such as *LRRC15*$^{+}$ populations) remains to be fully elucidated. Future studies utilizing high-depth spatial transcriptomics will be necessary to overcome the detection limits of standard scRNA-seq and map the spatial dynamics of *MRGPRX2*$^{+}$ fibroblasts during fibrotic progression.

Fibroblasts have traditionally been viewed as passive structural cells responsible for maintaining ECM integrity.[50,51] However, upon exposure to external insults, such as tissue injury, inflammation, or chronic stress, fibroblasts become activated, transformed into myofibroblasts, and actively contribute to wound healing and fibrotic processes.[52–56] A key driver of this transition is the dynamic crosstalk between fibroblasts and immune cells, particularly macrophages.[36,57–59] Activated macrophages secrete factors such as TGF-β, PDGF, and Relm, which promote fibroblast proliferation and activation.[35,60–62] In turn, fibroblasts produce chemokines such as CCL2 and cytokines such as IL-6, facilitating macrophage recruitment and activation and sustaining the inflammatory and fibrotic milieu.[63,64] This bidirectional communication highlights the evolving role of fibroblasts from passive ECM producers to active regulators of immune responses and tissue remodeling. Notably, while mast cells can modulate immune cell recruitment through MrgprB2-dependent degranulation, our data showing preserved fibrosis in mast cell-deficient mice underscore that the direct LL37-MrgprB2 axis in fibroblasts is the dominant driver of fibrotic remodeling, independent of mast cell-mediated inflammatory amplification. Notably, this transformation is further marked by the upregulation of MrgprX2/MrgprB2 in fibroblasts, which equips them to directly sense damage-associated signals and promote rapid wound repair. However, in the presence of sustained LL37 release and unresolved inflammation, this fibroblast-intrinsic immune surveillance system may become maladaptive, driving excessive fibroblast proliferation, myofibroblast differentiation, and fibrotic remodeling. Our findings thus position MrgprX2/B2 as a novel component bridging the skin's neuroendocrine network with fibrotic pathology through Ca^{2+}-calcineurin-NFAT-TGF-β1 signaling,[15] aligning with the emerging view of fibroblasts as active neuroendocrine participants.[65] Despite known differences in steroidogenic regulation and anatomical structure between mouse and human skin,[65] the functional conservation of the MrgprX2/B2 pathway across species is validated through human tissue analysis, mouse genetic models, and humanized skin organoids to support its translational relevance for therapeutic targeting in HTS.

In summary, this study highlights the critical role of MrgprX2/MrgprB2^{+} fibroblasts in mediating skin fibrosis. The upregulation of MrgprX2/MrgprB2 under pathological conditions underscores its contribution to fibroblast activation and the progression of fibrosis in both human and murine models. Our findings provide important insights into the cellular and molecular mechanisms underlying pathological fibrosis and suggest that targeting MrgprX2/MrgprB2 may offer a novel therapeutic strategy to enhance wound healing and mitigate HTS.

Limitations of the study

While this study identifies MrgprX2/B2 as a critical driver of fibroblast-mediated fibrosis, and our LL37-induced mouse model has proven effective for mechanistic dissection, future research must enhance its translational and clinical relevance. To better correlate with human data and validate findings, developing humanized MrgprX2 receptor mouse models is crucial, especially given the species-specific differences between human MrgprX2 and mouse MrgprB2. A deeper understanding of the functional distinctions between MrgprX2 and MrgprB2 is also essential to refine therapeutic targets and ensure drug specificity. Furthermore, these models, along with robust cell-based assays, can be leveraged for pharmacological validation and accelerated drug development, including screening novel antagonists with high selectivity and potency. Integrating these advanced models with human clinical data, considering factors such as genetic polymorphisms, will significantly advance our understanding and the development of targeted therapies for fibrotic diseases.

Several conceptual considerations also remain. The *COL1A2*^{creER} driver targets a broad fibroblast population, and while our findings establish a clear role for fibroblast-expressed

MrgprX2/B2 in fibrosis, the precise subset responsible awaits further resolution. The partial uncoupling of MrgprX2 expression from the LRRC15^{+} lineage suggests that MrgprX2^{+} cells occupy a functionally distinct activation state. Emerging technologies such as high-depth spatial transcriptomics will be instrumental in mapping the identity and spatial dynamics of this population with greater specificity. Finally, the humanized 3D organoid model, despite its considerable strengths, lacks vasculature, immune infiltrates, and innervation; next-generation organoid platforms incorporating these components will provide an even more complete recapitulation of the fibrotic microenvironment. These constraints notwithstanding, convergent evidence from human tissues, multiple mouse genetic models, and organoid systems collectively supports MrgprX2/B2 as a promising therapeutic target in HTS.

RESOURCE AVAILABILITY

Lead contact

- Requests for further information and resources should be directed to and will be fulfilled by the lead contact, Heng Xu (xuh1990@gmail.com).

Materials availability

- All unique/stable reagents generated in this study are available from the lead contact with a completed materials transfer agreement.

Data and code availability

The raw data from whole-genome sequencing have been deposited in the NCBI Sequence Read Archive (SRA), with accession code PRJNA1259902. This paper does not report original code. Any additional information required to reanalyze the data reported in this paper is available from the lead contact upon request.

ACKNOWLEDGMENTS

We appreciate the insightful discussions with Zeyu Chen at Peking University School of Basic Medical Sciences. We thank Lei Zhang at Shanghai Institute of Materia Medica for providing technical support in data analysis. We thank Yanke Wang at the National Facility for Protein Science in Shanghai for providing technical support and assistance in data collection and analysis. This work was supported by Strategic Priority Research Program of the Chinese Academy of Sciences grant no. XDB1060000 (J.F.), National Key Research and Development Program of China grant no. 2024YFC3505305 (J.F.), National Natural Science Foundation of China grant no. 82572881 (H.X.), National Natural Science Foundation of China grant nos. 82571383, 82171214, and 32241003 (J.F.), Shanghai Health Industry Clinical Research Special Project 20224Y0146, Shanghai Rising-Star Program grant no. 24QB2701200 (H.X.), Shanghai "Rising Stars of Medical Talents" Youth Development Program SHWSRS (2023)_26 (H.X.), National Natural Science Foundation of China grant nos. U24A20783 and 82471233 (T.W.), Shanghai Municipal Natural Science Foundation grant no. 23ZR1474500 (J.F.), State Key Laboratory of Chemical Biology grant no. SKLCB-2025-02 (J.F.), Noncommunicable Chronic Diseases-National Science and Technology Major Project, 2026ZD0552704 (J.F.), and supports from the Lingang Laboratory, grant nos. LG-QS-202203-07 and LGL-2614-10 (J.F.).

AUTHOR CONTRIBUTIONS

Conceptualization, H.X., J.F., Y.L., and Y.Z.; methodology, T.W., J.F., H.X., and L.Z.; investigation, H.X., M.S., Y.J., Y.L., L.W., Z.W., J.S., T.S., and L.Z.; writing – original draft, J.F. and H.X.; writing – review and editing, J.F. and H.X.; funding acquisition, T.W., H.X., and J.F.; resources, T.W., J.F., and H.X.; supervision, J.F., H.X., and Y.Z.

DECLARATION OF INTERESTS

The authors declare no competing interests.

STAR★METHODS

Detailed methods are provided in the online version of this paper and include the following:

- KEY RESOURCES TABLE
- EXPERIMENTAL MODEL AND STUDY PARTICIPANT DETAILS
  - Human participants
  - Animals
  - Cell lines
- METHOD DETAILS
  - Mouse model of hypertrophic scar
  - LL37-induced fibrosis and pharmacological intervention
  - Mouse model of full-thickness wounding
  - Bleomycin-induced fibrosis model
  - Reconstructed full-thickness human skin organoid model
  - Preparation of primary human fibroblasts
  - Preparation of primary mouse fibroblasts
  - Cell viability assays
  - siRNA-mediated gene silencing
  - Plasmid construction and transfection
  - Live-cell Ca^{2+} imaging
  - RNA extraction and RT-qPCR
  - Western Blot
  - Flow cytometry
  - RNAscope in situ hybridization
  - Histology analysis
  - RNA-seq analysis
  - scRNA-seq analysis
- QUANTIFICATION AND STATISTICAL ANALYSIS

SUPPLEMENTAL INFORMATION

Supplemental information can be found online at https://doi.org/10.1016/j.celrep.2026.117616.

Received: September 16, 2025
Revised: April 8, 2026
Accepted: June 9, 2026
Published: June 25, 2026

REFERENCES

1. Martin, P., Pardo-Pastor, C., Jenkins, R.G., and Rosenblatt, J. (2024). Imperfect wound healing sets the stage for chronic diseases. Science *386*, eadp2974. https://doi.org/10.1126/science.adp2974.
2. Limandjaja, G.C., Niessen, F.B., Scheper, R.J., and Gibbs, S. (2021). Hypertrophic scars and keloids: Overview of the evidence and practical guide for differentiating between these abnormal scars. Exp. Dermatol. *30*, 146–161. https://doi.org/10.1111/exd.14121.
3. Rössler, S., Nischwitz, S.P., Luze, H., Holzer-Geissler, J.C.J., Zrim, R., and Kamolz, L.P. (2022). In Vivo Models for Hypertrophic Scars-A Systematic Review. Medicina (Kaunas) *58*, 736. https://doi.org/10.3390/medicina58060736.
4. Mustoe, T.A., Cooter, R.D., Gold, M.H., Richard Hobbs, F.D., Ramelet, A.A., Shakespeare, P.G., Stella, M., Téot, L., Wood, F.M., and Ziegler, U.E. (2002). International clinical recommendations on scar management. Plast. Reconstr. Surg. *110*, 560–571. https://doi.org/10.1097/00006534-200208000-00031.
5. Zhang, J., Li, Y., Bai, X., Li, Y., Shi, J., and Hu, D. (2018). Recent advances in hypertrophic scar. Histol. Histopathol. *33*, 27–39. https://doi.org/10.14670/hh-11-908.

6. Sinha, S., Sparks, H.D., Labit, E., Robbins, H.N., Gowing, K., Jaffer, A., Kutluberk, E., Arora, R., Raredon, M.S.B., Cao, L., et al. (2022). Fibroblast inflammatory priming determines regenerative versus fibrotic skin repair in reindeer. Cell *185*, 4717–4736.e25. https://doi.org/10.1016/j.cell.2022.11.004.

7. Talbott, H.E., Mascharak, S., Griffin, M., Wan, D.C., and Longaker, M.T. (2022). Wound healing, fibroblast heterogeneity, and fibrosis. Cell Stem Cell *29*, 1161–1180. https://doi.org/10.1016/j.stem.2022.07.006.

8. Bagabir, R., Byers, R.J., Chaudhry, I.H., Müller, W., Paus, R., and Bayat, A. (2012). Site-specific immunophenotyping of keloid disease demonstrates immune upregulation and the presence of lymphoid aggregates. Br. J. Dermatol. *167*, 1053–1066. https://doi.org/10.1111/j.1365-2133.2012.11190.x.

9. Shih, B., and Bayat, A. (2010). Genetics of keloid scarring. Arch. Dermatol. Res. *302*, 319–339. https://doi.org/10.1007/s00403-009-1014-y.

10. Fu, X., Khalil, H., Kanisicak, O., Boyer, J.G., Vagnozzi, R.J., Maliken, B.D., Sargent, M.A., Prasad, V., Valiente-Alandi, I., Blaxall, B.C., and Molkentin, J.D. (2018). Specialized fibroblast differentiated states underlie scar formation in the infarcted mouse heart. J. Clin. Investig. *128*, 2127–2143. https://doi.org/10.1172/jci98215.

11. Shook, B.A., Wasko, R.R., Rivera-Gonzalez, G.C., Salazar-Gatzimas, E., López-Giráldez, F., Dash, B.C., Muñoz-Rojas, A.R., Aultman, K.D., Zwick, R.K., Lei, V., et al. (2018). Myofibroblast proliferation and heterogeneity are supported by macrophages during skin repair. Science *362*, eaar2971. https://doi.org/10.1126/science.aar2971.

12. Tauber, M., Basso, L., Martin, J., Bostan, L., Pinto, M.M., Thierry, G.R., Houmadi, R., Serhan, N., Loste, A., Blériot, C., et al. (2023). Landscape of mast cell populations across organs in mice and humans. J. Exp. Med. *220*, e20230570. https://doi.org/10.1084/jem.20230570.

13. Mascharak, S., desJardins-Park, H.E., Davitt, M.F., Griffin, M., Borrelli, M.R., Moore, A.L., Chen, K., Duoto, B., Chinta, M., Foster, D.S., et al. (2021). Preventing Engrailed-1 activation in fibroblasts yields wound regeneration without scarring. Science *372*, eaba2374. https://doi.org/10.1126/science.aba2374.

14. Younesi, F.S., Miller, A.E., Barker, T.H., Rossi, F.M.V., and Hinz, B. (2024). Fibroblast and myofibroblast activation in normal tissue repair and fibrosis. Nat. Rev. Mol. Cell Biol. *25*, 617–638. https://doi.org/10.1038/s41580-024-00716-0.

15. Slominski, R.M., Raman, C., Jetten, A.M., and Slominski, A.T. (2025). Neuro-immuno-endocrinology of the skin: how environment regulates body homeostasis. Nat. Rev. Endocrinol. *21*, 495–509. https://doi.org/10.1038/s41574-025-01107-x.

16. Kühn, H., Kolkhir, P., Babina, M., Düll, M., Frischbutter, S., Fok, J.S., Jiao, Q., Metz, M., Scheffel, J., Wolf, K., et al. (2021). Mas-related G protein-coupled receptor X2 and its activators in dermatologic allergies. J. Allergy Clin. Immunol. *147*, 456–469. https://doi.org/10.1016/j.jaci.2020.08.027.

17. McNeil, B.D., Pundir, P., Meeker, S., Han, L., Undem, B.J., Kulka, M., and Dong, X. (2015). Identification of a mast-cell-specific receptor crucial for pseudo-allergic drug reactions. Nature *519*, 237–241. https://doi.org/10.1038/nature14022.

18. Motakis, E., Guhl, S., Ishizu, Y., Itoh, M., Kawaji, H., de Hoon, M., Lassmann, T., Carninci, P., Hayashizaki, Y., Zuberbier, T., et al. (2014). Redefinition of the human mast cell transcriptome by deep-CAGE sequencing. Blood *123*, e58–e67. https://doi.org/10.1182/blood-2013-02-483792.

19. Pundir, P., Liu, R., Vasavda, C., Serhan, N., Limjunyawong, N., Yee, R., Zhan, Y., Dong, X., Wu, X., Zhang, Y., et al. (2019). A Connective Tissue Mast-Cell-Specific Receptor Detects Bacterial Quorum-Sensing Molecules and Mediates Antibacterial Immunity. Cell Host Microbe *26*, 114–122.e8. https://doi.org/10.1016/j.chom.2019.06.003.

20. Cao, C., and Roth, B.L. (2023). The structure, function, and pharmacology of MRGPRs. Trends Pharmacol. Sci. *44*, 237–251. https://doi.org/10.1016/j.tips.2023.02.002.

21. Gour, N., and Dong, X. (2024). The MRGPR family of receptors in immunity. Immunity *57*, 28–39. https://doi.org/10.1016/j.immuni.2023.12.012.

22. Meixiong, J., Anderson, M., Limjunyawong, N., Sabbagh, M.F., Hu, E., Mack, M.R., Oetjen, L.K., Wang, F., Kim, B.S., and Dong, X. (2019). Activation of Mast-Cell-Expressed Mas-Related G-Protein-Coupled Receptors Drives Non-histaminergic Itch. Immunity *50*, 1163–1171.e5. https://doi.org/10.1016/j.immuni.2019.03.013.

23. Son, H., Zhang, Y., Shannonhouse, J., Ishida, H., Gomez, R., and Kim, Y.S. (2024). Mast-cell-specific receptor mediates alcohol-withdrawal-associated headache in male mice. Neuron *112*, 113–123.e4. https://doi.org/10.1016/j.neuron.2023.09.039.

24. Chen, E., Chuang, L.S., Giri, M., Villaverde, N., Hsu, N.Y., Sabic, K., Joshowitz, S., Gettler, K., Nayar, S., Chai, Z., et al. (2021). Inflamed Ulcerative Colitis Regions Associated With MRGPRX2-Mediated Mast Cell Degranulation and Cell Activation Modules, Defining a New Therapeutic Target. Gastroenterology *160*, 1709–1724. https://doi.org/10.1053/j.gastro.2020.12.076.

25. Roy, S., Chompunud Na Ayudhya, C., Thapaliya, M., Deepak, V., and Ali, H. (2021). Multifaceted MRGPRX2: New insight into the role of mast cells in health and disease. J. Allergy Clin. Immunol. *148*, 293–308. https://doi.org/10.1016/j.jaci.2021.03.049.

26. Zhang, S., Edwards, T.N., Chaudhri, V.K., Wu, J., Cohen, J.A., Hirai, T., Rittenhouse, N., Schmitz, E.G., Zhou, P.Y., McNeil, B.D., et al. (2021). Nonpeptidergic neurons suppress mast cells via glutamate to maintain skin homeostasis. Cell *184*, 2151–2166.e16. https://doi.org/10.1016/j.cell.2021.03.002.

27. Lim, Y.W., Quinn, R., Bharti, K., Ferrer, M., Zarkoob, H., and Song, M.J. (2024). Development of immunocompetent full thickness skin tissue constructs to model skin fibrosis for high-throughput drug screening. Biofabrication *17*, 015033. https://doi.org/10.1088/1758-5090/ad998c.

28. Sharma, A.N., Birda, A., Park, M., Choe, S., Salas, J., Kincaid, C., and Mesinkovska, N.A. (2025). Insights Into Demographics, Comorbidities, and Risk Factors in Keloids and Hypertrophic Scars: A Retrospective Study. J. Drugs Dermatol. *24*, 212–215. https://doi.org/10.36849/jdd.8401.

29. Yang, F., Wang, L., Song, D., Zhang, L., Wang, X., Du, D., and Jiang, X. (2024). Signaling pathways and targeted therapy for rosacea. Front. Immunol. *15*, 1367994. https://doi.org/10.3389/fimmu.2024.1367994.

30. Morizane, S., Yamasaki, K., Mühleisen, B., Kotol, P.F., Murakami, M., Aoyama, Y., Iwatsuki, K., Hata, T., and Gallo, R.L. (2012). Cathelicidin antimicrobial peptide LL-37 in psoriasis enables keratinocyte reactivity against TLR9 ligands. J. Invest. Dermatol. *132*, 135–143. https://doi.org/10.1038/jid.2011.259.

31. Manabe, T., Park, H., and Minami, T. (2021). Calcineurin-nuclear factor for activated T cells (NFAT) signaling in pathophysiology of wound healing. Inflamm. Regen. *41*, 26. https://doi.org/10.1186/s41232-021-00176-5.

32. Santus, W., Barresi, S., Mingozzi, F., Broggi, A., Orlandi, I., Stamerra, G., Vai, M., Martorana, A.M., Polissi, A., Köhler, J.R., et al. (2017). Skin infections are eliminated by cooperation of the fibrinolytic and innate immune systems. Sci. Immunol. *2*, eaan2725. https://doi.org/10.1126/sciimmunol.aan2725.

33. Sengupta, S., Jana, S., and Bhattacharyya, A. (2014). TGF-β-Smad2 dependent activation of CDC 25A plays an important role in cell proliferation through NFAT activation in metastatic breast cancer cells. Cell. Signal. *26*, 240–252. https://doi.org/10.1016/j.cellsig.2013.11.013.

34. Yáñez-Bisbe, L., Moya, M., Rodríguez-Sinovas, A., Ruiz-Meana, M., Inserte, J., Tajes, M., Batlle, M., Guasch, E., Mas-Stachurska, A., Miró, E., et al. (2024). TRPV4 Channels Promote Pathological, but Not Physiological, Cardiac Remodeling through the Activation of Calcineurin/NFAT and TRPC6. Int. J. Mol. Sci. *25*, 1541. https://doi.org/10.3390/ijms25031541.

35. Amrute, J.M., Luo, X., Penna, V., Yang, S., Yamawaki, T., Hayat, S., Bredemeyer, A., Jung, I.H., Kadyrov, F.F., Heo, G.S., et al. (2024). Targeting immune-fibroblast cell communication in heart failure. Nature *635*, 423–433. https://doi.org/10.1038/s41586-024-08008-5.

36. Buechler, M.B., Fu, W., and Turley, S.J. (2021). Fibroblast-macrophage reciprocal interactions in health, fibrosis, and cancer. Immunity *54*, 903–915. https://doi.org/10.1016/j.immuni.2021.04.021.

37. Sawant, M., Wang, F., Koester, J., Niehoff, A., Nava, M.M., Lundgren-Akerlund, E., Gullberg, D., Leitinger, B., Wickström, S., Eckes, B., and Krieg, T. (2023). Ablation of integrin-mediated cell-collagen communication alleviates fibrosis. Ann. Rheum. Dis. *82*, 1474–1486. https://doi.org/10.1136/ard-2023-224129.

38. Zhou, X., Franklin, R.A., Adler, M., Jacox, J.B., Bailis, W., Shyer, J.A., Flavell, R.A., Mayo, A., Alon, U., and Medzhitov, R. (2018). Circuit Design Features of a Stable Two-Cell System. Cell *172*, 744–757.e17. https://doi.org/10.1016/j.cell.2018.01.015.

39. Dorschner, R.A., Pestonjamasp, V.K., Tamakuwala, S., Ohtake, T., Rudisill, J., Nizet, V., Agerberth, B., Gudmundsson, G.H., and Gallo, R.L. (2001). Cutaneous injury induces the release of cathelicidin anti-microbial peptides active against group A Streptococcus. J. Invest. Dermatol. *117*, 91–97. https://doi.org/10.1046/j.1523-1747.2001.01340.x.

40. Grönberg, A., Mahlapuu, M., Ståhle, M., Whately-Smith, C., and Rollman, O. (2014). Treatment with LL-37 is safe and effective in enhancing healing of hard-to-heal venous leg ulcers: a randomized, placebo-controlled clinical trial. Wound Repair Regen. *22*, 613–621. https://doi.org/10.1111/wrr.12211.

41. Schauber, J., Dorschner, R.A., Coda, A.B., Büchau, A.S., Liu, P.T., Kiken, D., Helfrich, Y.R., Kang, S., Elalieh, H.Z., Steinmeyer, A., et al. (2007). Injury enhances TLR2 function and antimicrobial peptide expression through a vitamin D-dependent mechanism. J. Clin. Investig. *117*, 803–811. https://doi.org/10.1172/jci30142.

42. Slominski, A.T., Kim, T.K., Janjetovic, Z., Slominski, R.M., Li, W., Jetten, A.M., Indra, A.K., Mason, R.S., and Tuckey, R.C. (2024). Biological Effects of CYP11A1-Derived Vitamin D and Lumisterol Metabolites in the Skin. J. Invest. Dermatol. *144*, 2145–2161. https://doi.org/10.1016/j.jid.2024.04.022.

43. Green, D.P., Limjunyawong, N., Gour, N., Pundir, P., and Dong, X. (2019). A Mast-Cell-Specific Receptor Mediates Neurogenic Inflammation and Pain. Neuron *101*, 412–420.e3. https://doi.org/10.1016/j.neuron.2019.01.012.

44. Mencarelli, A., Gunawan, M., Yong, K.S.M., Bist, P., Tan, W.W.S., Tan, S.Y., Liu, M., Huang, E.K., Fan, Y., Chan, J.K.Y., et al. (2020). A humanized mouse model to study mast cells mediated cutaneous adverse drug reactions. J. Leukoc. Biol. *107*, 797–807. https://doi.org/10.1002/jlb.3ma1219-210rr.

45. Lendahl, U., Muhl, L., and Betsholtz, C. (2022). Identification, discrimination and heterogeneity of fibroblasts. Nat. Commun. *13*, 3409. https://doi.org/10.1038/s41467-022-30633-9.

46. Arifuzzaman, M., Mobley, Y.R., Choi, H.W., Bist, P., Salinas, C.A., Brown, Z.D., Chen, S.L., Staats, H.F., and Abraham, S.N. (2019). MRGPR-mediated activation of local mast cells clears cutaneous bacterial infection and protects against reinfection. Sci. Adv. *5*, eaav0216. https://doi.org/10.1126/sciadv.aav0216.

47. Kolkhir, P., Pyatilova, P., Ashry, T., Jiao, Q., Abad-Perez, A.T., Altrichter, S., Vera Ayala, C.E., Church, M.K., He, J., Lohse, K., et al. (2022). Mast cells, cortistatin, and its receptor, MRGPRX2, are linked to the pathogenesis of chronic prurigo. J. Allergy Clin. Immunol. *149*, 1998–2009.e5. https://doi.org/10.1016/j.jaci.2022.02.021.

48. Subramanian, H., Gupta, K., and Ali, H. (2016). Roles of Mas-related G protein-coupled receptor X2 on mast cell-mediated host defense, pseudoallergic drug reactions, and chronic inflammatory diseases. J. Allergy Clin. Immunol. *138*, 700–710. https://doi.org/10.1016/j.jaci.2016.04.051.

49. Wedi, B., Gehring, M., and Kapp, A. (2020). The pseudoallergen receptor MRGPRX2 on peripheral blood basophils and eosinophils: Expression and function. Allergy *75*, 2229–2242. https://doi.org/10.1111/all.14213.

50. Driskell, R.R., and Watt, F.M. (2015). Understanding fibroblast heterogeneity in the skin. Trends Cell Biol. *25*, 92–99. https://doi.org/10.1016/j.tcb.2014.10.001.

51. Lynch, M.D., and Watt, F.M. (2018). Fibroblast heterogeneity: implications for human disease. J. Clin. Investig. *128*, 26–35. https://doi.org/10.1172/jci93555.

52. Koyama, Y., and Brenner, D.A. (2017). Liver inflammation and fibrosis. J. Clin. Investig. *127*, 55–64. https://doi.org/10.1172/jci88881.

53. Liu, M., López de Juan Abad, B., and Cheng, K. (2021). Cardiac fibrosis: Myofibroblast-mediated pathological regulation and drug delivery strategies. Adv. Drug Deliv. Rev. *173*, 504–519. https://doi.org/10.1016/j.addr.2021.03.021.

54. McLellan, M.A., Skelly, D.A., Dona, M.S.I., Squiers, G.T., Farrugia, G.E., Gaynor, T.L., Cohen, C.D., Pandey, R., Diep, H., Vinh, A., et al. (2020). High-Resolution Transcriptomic Profiling of the Heart During Chronic Stress Reveals Cellular Drivers of Cardiac Fibrosis and Hypertrophy. Circulation *142*, 1448–1463. https://doi.org/10.1161/circulationaha.119.045115.

55. Miguel, V., Shaw, I.W., and Kramann, R. (2025). Metabolism at the crossroads of inflammation and fibrosis in chronic kidney disease. Nat. Rev. Nephrol. *21*, 39–56. https://doi.org/10.1038/s41581-024-00889-z.

56. Plikus, M.V., Wang, X., Sinha, S., Forte, E., Thompson, S.M., Herzog, E.L., Driskell, R.R., Rosenthal, N., Biernaskie, J., and Horsley, V. (2021). Fibroblasts: Origins, definitions, and functions in health and disease. Cell *184*, 3852–3872. https://doi.org/10.1016/j.cell.2021.06.024.

57. Gao, Y., Li, J., Cheng, W., Diao, T., Liu, H., Bo, Y., Liu, C., Zhou, W., Chen, M., Zhang, Y., et al. (2024). Cross-tissue human fibroblast atlas reveals myofibroblast subtypes with distinct roles in immune modulation. Cancer Cell *42*, 1764–1783.e10. https://doi.org/10.1016/j.ccell.2024.08.020.

58. Peng, Y., Li, L., Shang, J., Zhu, H., Liao, J., Hong, X., Hou, F.F., Fu, H., and Liu, Y. (2023). Macrophage promotes fibroblast activation and kidney fibrosis by assembling a vitronectin-enriched microenvironment. Theranostics *13*, 3897–3913. https://doi.org/10.7150/thno.85250.

59. Simões, F.C., Cahill, T.J., Kenyon, A., Gavriouchkina, D., Vieira, J.M., Sun, X., Pezzolla, D., Ravaud, C., Masmanian, E., Weinberger, M., et al. (2020). Macrophages directly contribute collagen to scar formation during zebrafish heart regeneration and mouse heart repair. Nat. Commun. *11*, 600. https://doi.org/10.1038/s41467-019-14263-2.

60. Liu, W., Hardaway, B.D., Kim, E., Pauli, J., Wettich, J.L., Yalcinkaya, M., Hsu, C.C., Xiao, T., Reilly, M.P., Tabas, I., et al. (2024). Inflammatory cross-talk impairs phagocytic receptors and aggravates atherosclerosis in clonal hematopoiesis in mice. J. Clin. Investig. *135*, e182939. https://doi.org/10.1172/jci182939.

61. Qi, J., Sun, H., Zhang, Y., Wang, Z., Xun, Z., Li, Z., Ding, X., Bao, R., Hong, L., Jia, W., et al. (2022). Single-cell and spatial analysis reveal interaction of FAP(+) fibroblasts and SPP1(+) macrophages in colorectal cancer. Nat. Commun. *13*, 1742. https://doi.org/10.1038/s41467-022-29366-6.

62. Ueshima, E., Fujimori, M., Kodama, H., Felsen, D., Chen, J., Durack, J.C., Solomon, S.B., Coleman, J.A., and Srimathveeravalli, G. (2019). Macrophage-secreted TGF-β(1) contributes to fibroblast activation and ureteral stricture after ablation injury. Am J Physiol Renal Physiol *317*, F52–F64. https://doi.org/10.1152/ajprenal.00260.2018.

63. Kechagia, J.Z., Ezra, D.G., Burton, M.J., and Bailly, M. (2016). Fibroblasts profiling in scarring trachoma identifies IL-6 as a functional component of a fibroblast-macrophage pro-fibrotic and pro-inflammatory feedback loop. Sci. Rep. *6*, 28261. https://doi.org/10.1038/srep28261.

64. Ko, K.I., DerGarabedian, B.P., Chen, Z., Debnath, R., Ko, A., Link, B.N., Korostoff, J.M., and Graves, D.T. (2023). Distinct fibroblast progenitor subpopulation expedites regenerative mucosal healing by immunomodulation. J. Exp. Med. *220*, e20221350. https://doi.org/10.1084/jem.20221350.

65. Slominski, A.T., Manna, P.R., and Tuckey, R.C. (2015). On the role of skin in the regulation of local and systemic steroidogenic activities. Steroids *103*, 72–88. https://doi.org/10.1016/j.steroids.2015.04.006.

STAR★METHODS

KEY RESOURCES TABLE

REAGENT or RESOURCE	SOURCE	IDENTIFIER
Antibodies		
Rabbit Polyclonal anti-CAMP antibody	Proteintech	Cat# 12009-1-AP; RRID: AB_908736
Rabbit Polyclonal anti-MRGPRX2 antibody	Abcam	Cat# ab237047; RRID: AB_10782580
Rabbit Monoclonal anti-COL1A1 antibody	HuaBio	Cat# HA722517; RRID: AB_3714533
Mouse Monoclonal anti-alpha smooth muscle Actin antibody	Abcam	Cat# ab7817; RRID: AB_262054
Rabbit Monoclonal anti-Ki67 antibody	Affinity	Cat# AF0198; RRID: AB_2834152
Mouse Monoclonal anti-TGF beta-1 antibody	Thermo Fisher Scientific	Cat# MA1-21595; RRID: AB_561657
Rabbit Polyclonal anti-GAPDH antibody	Proteintech	Cat# 10494-1-AP; RRID: AB_2263076
Mouse Monoclonal anti-Beta Actin antibody	Proteintech	Cat# 66009-1-Ig; RRID: AB_2687938
Rabbit Monoclonal anti-COL3A1 antibody	HuaBio	Cat# HA720050; RRID: AB_3071990
Mouse Monoclonal anti-Periostin antibody	Proteintech	Cat# 66491-1-Ig; RRID: AB_2881856
Rabbit Polyclonal anti-Keratin 14 Antibody	BioLegend	Cat# 905304; RRID: AB_2616896
Mouse monoclonal anti-Avidin–FITC antibody	Sigma-Aldrich	Cat# F1269; RRID: AB_259431
Rabbit Polyclonal anti-MPO antibody	Proteintech	Cat# 22225-1-AP; RRID: AB_2879037
Rabbit Polyclonal anti-FAP antibody	ABclonal	Cat# A6349; RRID: AB_2766951
Rabbit Monoclonal anti-COL1A2 antibody	Abcam	Cat# ab308455; RRID: AB_3678665
Mouse monoclonal anti-NFATc1 antibody	Santa Cruz Biotechnology	Cat# sc-7294; RRID: AB_2152503
Rat monoclonal anti-ER-TR7 antibody	Santa Cruz Biotechnology	Cat# sc-73355; RRID: AB_1122890
Goat polyclonal AF488 Anti-Rabbit IgG antibody	Jackson ImmunoResearch Laboratories	Cat# 111-545-003; RRID: AB_2338046
Rabbit polyclonal Cy3 Anti-Mouse IgG antibody	Jackson ImmunoResearch Laboratories	Cat# 315-165-003; RRID: AB_2340135
Goat polyclonal AF647 Anti-Rabbit IgG antibody	Jackson ImmunoResearch Laboratories	Cat# 111-605-003 ; RRID: AB_2338072
Rat monoclonal BV605 Anti-Ly-6C antibody	BD Biosciences	Cat# 563011; RRID: AB_2737949
Rat monoclonal APC anti-Ly-6G antibody	BD Biosciences	Cat# 560600; RRID: AB_1727561
Rat monoclonal BB515 anti-CD11b antibody	BD Biosciences	Cat# 564454; RRID: AB_2665392
Rat monoclonal RB780 anti-CD45R/B220 antibody	BD Biosciences	Cat# 569208; RRID: AB_3684868
Rat monoclonal BV786 anti-CD335 (NKp46) antibody	BD Biosciences	Cat# 741029; RRID: AB_2740647
Rat monoclonal BV421 anti-CD117 (c-Kit) antibody	Biolegend	Cat# 105827; RRID: AB_10898120
Rat monoclonal RB705 anti-CD45 antibody	BD Biosciences	Cat# 570291; RRID: AB_3086726
Rat monoclonal PE anti-F4/80 antibody	BD Biosciences	Cat# 565410; RRID: AB_2687527
Rat monoclonal APC anti-CD3e antibody	BD Biosciences	Cat# 557596; RRID: AB_396759
Chemicals, peptides, and recombinant proteins		
LL37 peptides	Sangon Biotech(Shanghai)	Cat# P34103
Normal Donkey Serum	Millipore Sigma	Cat# 566460
Fetal Bovine Serum	Thermo Fisher Scientific	Cat# A5256701
Dulbecco's Modified Eagle Medium	Thermo Fisher Scientific	Cat# 11965092
RPMI-1640 Medium	Millipore Sigma	Cat# R8758
Penicillin-Streptomycin	Millipore Sigma	Cat# P0781
Collagenase NB4	Nordmark	Cat# S1745401
collagenase D	Millipore Sigma	Cat# 11088858001
Protease from *Streptomyces griseus*	Millipore Sigma	Cat# P5147
Paraformaldehyde Solution, 4% in PBS	Millipore Sigma	Cat# 30525-89-4

(*Continued on next page*)

Continued

REAGENT or RESOURCE	SOURCE	IDENTIFIER
Triton X-100	Millipore Sigma	Cat# X100
Cyclosporin A	Med chem express	Cat# HY-B0579
Bleomycin sulfate	Med chem express	Cat# HY-17565
Fura-2 AM	Millipore Sigma	Cat# 47989
Ionomycin	Yeasen	Cat# 50401ES03
Corn oil	Millipore Sigma	Cat# C8267
Dimethyl sulfoxide(DMSO)	Millipore Sigma	Cat# 67-68-5
Poly-L-Lysine Hydrobromide	Millipore Sigma	Cat# P4707
RIPA Lysis and Extraction Buffer	Thermo Fisher Scientific	Cat# 89901
1x Tris-Buffered Saline (TBS)	Biorad	Cat# 1610782
NuPAGE™ 4 to 12%, Bis-Tris, 1.0–1.5 mm	Thermo Fisher Scientific	Cat# NP0321BOX
NuPAGE™ MOPS SDS Running Buffer (20X)	Thermo Fisher Scientific	Cat# NP0001
NuPAGE™ Transfer Buffer (20X)	Thermo Fisher Scientific	Cat# NP00061
ChamQ Universal SYBR qPCR Master Mix	Vazyme	Cat# Q711-02
4′,6-Diamidino-2-phenylindole dihydrochloride (DAPI)	Millipore Sigma	Cat# MBD0020
MCDB 153 Medium	Sigma-Aldrich	Cat# M7403
Human Serum Albumin	Sigma-Aldrich	Cat# A9731
EGF	R&D Systems	Cat# 236-EG
KGF	R&D Systems	Cat# 251-KG
FGF	R&D Systems	Cat# 233-FB
Hydrocortisone	Sigma-Aldrich	Cat# H0888
Insulin	Sigma-Aldrich	Cat# I2643
Transferrin	Sigma-Aldrich	Cat# T8158
Tamoxifen	Millipore Sigma	Cat# 10540-29-1
Fixable Viability Stain 510	BD Biosciences	Cat# 564406; RRID: AB_2869572
Trypsin-EDTA (0.25%), phenol red	Gibco	Cat# 25200056
Critical commercial assays		
Cell Count Kit-8	Yeasen	Cat# 40203ES
HighGene transfection reagent	ABclonal Technology	Cat# RM09014
HyperScript III RT SuperMix for qPCR with gDNA Remover	EnzyArtisan	Cat# R202-02
RNAscope Multiplex Fluorescent Reagent Kit v2	Advanced Cell Diagnostics	Cat# 322300-USM
Bicinchoninic Acid (BCA) Protein Assay Kit	Thermo Scientific	Cat# 23225
Deposited data		
Bulk RNA-seq raw data	NCBI Sequence Read Archive (SRA)	PRJNA1259902: https://dataview.ncbi.nlm.nih.gov/object/PRJNA1259902?reviewer=nbfn6r9ebim28ea87amaid4skb
Experimental models: cell lines		
HFF1 Cell Line	STEM RECELL	Cat# STM-CL-5013
Primary Human Epidermal Keratinocytes	Lifeline Cell Technology	Cat# FC-0025
Primary Human Dermal Fibroblasts	Lifeline Cell Technology	Cat# FC-0024
Experimental models: organisms/strains		
Mouse: C57BL/6J	The Jackson Laboratory	Cat# 000664; RRID:IMSR_JAX:000664
Mouse: *MRGPRB2*$^{fl/fl}$	GemPharmatech	Cat# T009283
Mouse: *TGFB1*$^{fl/fl}$	The Jackson Laboratory	Cat# 002220 RRID:IMSR_JAX:002220
Mouse: *COL1A2*^{creER}	The Jackson Laboratory	Cat# 029235 RRID:IMSR_JAX:029235

(*Continued on next page*)

Continued		
REAGENT or RESOURCE	SOURCE	IDENTIFIER
Mouse: *MRGPRB2*^{cre}	GemPharmatech	Cat# T065301
Mouse: *Ai9* (tdTomato knock-in)	GemPharmatech	Cat# T002249
Mouse: B6.Cg-*Kit*$^{W\text{-}sh}$	The Jackson Laboratory	Cat #:030764 RRID:IMSR_JAX:030764
Mouse: *MRGPRB2*$^{-/-}$	Cyagen	Cat# S-KO-07487
Oligonucleotides		
MRGPRB2−mouse-siRNA	Obio	N/A
MRGPRX2−human−siRNA	Obio	N/A
Quantitative real-time PCR primers	Sangon Biotech(Shanghai)	N/A
Recombinant DNA		
LV-h-*MRGPRX2*-3flag	Hanbio Biotechnology	N/A
LV-*m*-*MRGPRB2*-3flag	Hanbio Biotechnology	N/A
Software and algorithms		
Prism	https://www.graphpad.com/scientific-software/prism/	N/A
ImageJ	https://imagej.nih.gov/ij/	N/A
FlowJo	https://www.flowjo.com	N/A
LAS X imaging software	Leica Microsystems	N/A
Adobe Photoshop	Adobe.com	N/A
Adobe Illustrator	Adobe.com	N/A

EXPERIMENTAL MODEL AND STUDY PARTICIPANT DETAILS

Human participants

Human skin tissue samples were collected from healthy donors and patients with pathological scars at the Ninth People's Hospital affiliated to Shanghai Jiao Tong University School of Medicine, following approval by the Institutional Review Board (IRB) (Approval No. SH9H-2022-T327-1). Pathological scar tissues were obtained from patients undergoing surgical excision. All tissue collections were performed under sterile conditions and processed for primary fibroblast isolation, histological analysis, or cryopreservation at −80°C for subsequent immunofluorescence staining. Written informed consent was obtained from all participants prior to sample collection, in accordance with the Declaration of Helsinki.

Animals

All animal experiments were conducted using male and female mice aged 8–10 weeks at the initiation of experiments. The strains used included wild-type C57BL/6J mice (The Jackson Laboratory, Cat# 000664; RRID: IMSR_JAX:000664), *MRGPRB2*$^{fl/fl}$ mice (GemPharmatech, Cat# T009283), *TGFB1*$^{fl/fl}$ mice (The Jackson Laboratory, Cat# 002220; RRID: IMSR_JAX:002220), *COL1A2*^{creER} mice (The Jackson Laboratory, Cat# 029235; RRID: IMSR_JAX:029235), *MRGPRB2*^{cre} mice (GemPharmatech, Cat# T065301), Ai9 tdTomato knock-in reporter mice (GemPharmatech, Cat# T002249), mast cell-deficient B6.Cg-*Kit*$^{W\text{-}sh}$ mice (The Jackson Laboratory, Cat# 030764; RRID: IMSR_JAX:030764), and global *MRGPRB2*$^{-/-}$ knockout mice (Cyagen, Cat# S-KO-07487). Both sexes were used in the LL37-induced fibrosis model (Figures 4A–4F, 5B, 5C, 5N–5V, 6I–6N, S7, S8, S9, and S10), while male mice were used exclusively for primary cell isolation and *in vitro* experiments. No significant sex-dependent differences in lesion severity or fibrotic markers were observed in the LL37-induced fibrosis model. All animals were housed in specific pathogen-free (SPF) conditions under a controlled environment with a 12-h light/dark cycle, constant temperature (24°C), and free access to food and water. All animal experimental procedures were conducted in strict accordance with the guidelines of the National Institutes of Health Guide for the Care and Use of Laboratory Animals and approved by the Institutional Animal Care and Use Committee of the Shanghai Institute of Materia Medica, Chinese Academy of Sciences. Procedures were approved by the Experimental Animal Management Committee (IACUC), Shanghai Institute of Materia Medica, Chinese Academy of Sciences, according to all external and internal biosafety and bioethics guidelines (Ethics No. 2023-04-FJ-009).

Cell lines

The HFF1 human foreskin fibroblast cell line (STEM RECELL, Cat# STM-CL-5013) was used for MrgprX2 overexpression experiments. Primary Human Epidermal Keratinocytes (Lifeline Cell Technology, Cat# FC-0025) and Primary Human Dermal Fibroblasts (Lifeline Cell Technology, Cat# FC-0024) were used for the construction of the humanized full-thickness 3D skin organoid model.

METHOD DETAILS

Mouse model of hypertrophic scar

To establish a reproducible mouse model of hypertrophic scar (HTS), LL37 peptide was used as a proinflammatory and pro-fibrotic stimulus. Male and female mice (8–10 weeks old, weighing 22–25 g) were anesthetized, and the dorsal skin was shaved to expose a 1 cm × 1 cm area. A volume of 50 μL of 640 μM LL37 peptide dissolved in PBS was intradermally injected into the center of the marked area once daily for 21 consecutive days. Photographs of the treated site were taken prior to each injection to monitor gross morphological changes. Skin samples were harvested at baseline (day 0) and on days 3, 7, and 21 post-initial injection for histological, molecular, and cellular analyses. No significant sex-dependent differences in lesion severity or fibrotic markers were observed. This model recapitulates key features of human HTS, including dermal thickening, collagen deposition, and fibroblast activation.

LL37-induced fibrosis and pharmacological intervention

To evaluate the contribution of calcineurin signaling to LL37-mediated fibrosis, mice were treated with Cyclosporine A (CsA), a selective calcineurin inhibitor. Following the establishment of the LL37-induced fibrosis model (as described above), a treatment cocktail was prepared by incorporating a concentrated Cyclosporine A (CsA) stock solution (50 mg/mL) into the 640 μM LL37 solution at a final volume ratio of 1% (v/v). Subjects were administered a 50 μL intradermal injection of this mixture daily. Vehicle-treated controls received equivalent volumes of sterile saline.

Mouse model of full-thickness wounding

Telogen-phase mice (P50-P65) were anesthetized with isoflurane, and dorsal hair was removed using electric clippers. Following disinfection with 70% ethanol, full-thickness excisional wounds were created using sterile 6 mm biopsy punches (depending on experimental design). To minimize wound contraction and isolate re-epithelialization-mediated healing, the fascia layer beneath the panniculus carnosus was carefully excised around the wound perimeter. Wounds were left unsutured and covered with a transparent adhesive dressing (Tegaderm) to maintain hydration. The healing process was monitored longitudinally, with digital photographs captured at days 1, 3, 5, 7, and 9 post-wounding. Wound area was quantified using ImageJ software, and the percentage of wound closure was calculated as: final area/initial area × 100%.

Bleomycin-induced fibrosis model

To induce cutaneous fibrosis, mice received intradermal injections of bleomycin at a concentration of 1 unit/mL. A total volume of 100 μL was divided equally and administered across four symmetrical injection sites on the shaved dorsal skin. Injections were repeated every other day for a total of 14 days to establish reproducible fibrotic lesions. Control mice received equivalent volumes of sterile PBS following the same injection schedule. Skin samples were harvested 24–48 h after the final injection for histological and molecular characterization of fibrotic changes.

Reconstructed full-thickness human skin organoid model

A reconstructed full-thickness human skin organoid model was established to mimic the human skin microenvironment *in vitro*, based on modified protocols as previously described.[27] Primary human epidermal keratinocytes and dermal fibroblasts were obtained from Lifeline Technology. Cells were maintained in a specialized complete culture medium developed by Archgene Biotechnology Co., Ltd (Patent No. CN202111073240.0), consisting of MCDB153/DMEM supplemented with 10% FBS, 40 mg/mL human serum albumin, 10 ng/mL EGF, 10 ng/mL KGF, 10 ng/mL FGF, 500 ng/mL hydrocortisone, 5 μg/mL insulin, and 10 μg/mL transferrin.

To reconstruct the dermal layer, primary fibroblasts were suspended in a neutralized collagen type I solution (Sigma-Aldrich), poured into cell culture inserts, and incubated at 37°C for 3 days to allow polymerization and fibroblast spreading. Following dermal layer formation, primary keratinocytes were seeded onto the surface of the collagen-fibroblast gel and maintained under submerged conditions for an additional 3 days to promote cell attachment and initial stratification.

Subsequently, the cultures were exposed to an air-liquid interface by removing the apical medium, allowing the keratinocytes to differentiate and form a well-organized, multi-layered epidermis over the dermal equivalent. The reconstructed skin organoids were cultured for up to 14 days at the air-liquid interface, generating a full-thickness human skin structure consisting of a fibroblast-populated dermal layer and a stratified keratinocyte-derived epidermal layer. This humanized skin organoid model recapitulates key features of native human skin architecture and was utilized for subsequent functional and molecular analyses.

Preparation of primary human fibroblasts

Primary fibroblasts were isolated from normal human skin or pathological scar tissues. Fresh tissues were first rinsed in sterile PBS containing 1% Penicillin-Streptomycin (P/S) for 5-10 min to minimize microbial contamination. After drying, the tissues were minced into small fragments (approximately 1 mm^3) and subjected to enzymatic digestion with 0.3% Collagenase NB4 dissolved in DMEM. The digestion was performed at 37°C in a shaking incubator at 200 rpm for 3 h to release fibroblasts from the extracellular matrix.

The resulting cell suspension was filtered through a 70 μm cell strainer to remove undigested tissue fragments, and the filtrate was centrifuged twice at 1500 rpm for 5 min. The cell pellets were resuspended in DMEM supplemented with 10% fetal bovine serum and 1% P/S. The isolated fibroblasts were seeded into culture dishes, 6-well, 24-well, or 96-well plates, or on sterile glass coverslips for

subsequent experiments. Cells were maintained in a humidified incubator at 37°C with 5% CO_2. The culture medium was replaced every other day, and fibroblasts were used for experiments once the confluency reached 75% or higher.

Preparation of primary mouse fibroblasts

Primary dermal fibroblasts were isolated from full-thickness dorsal skin of male mice aged 8–10 weeks (with or without hypertrophic scar modeling). The harvested skin was rinsed with sterile PBS containing 1% P/S for 5–10 min. After drying, the tissue was minced into small fragments and digested in a solution containing Collagenase D and Streptomyces protease in RPMI 1640 medium. The digestion was performed at 37°C in a shaking incubator at 200 rpm for 90 min.

The digested mixture was filtered through a 70 μm cell strainer to obtain a single-cell suspension, followed by centrifugation twice at 580g for 7 min. The resulting cell pellet was resuspended in RPMI 1640 medium supplemented with 10% FBS and 1% P/S. The isolated fibroblasts were plated in appropriate culture dishes or plates and maintained at 37°C with 5% CO_2. The culture medium was refreshed every other day, and fibroblasts were collected for experiments when the cell confluency exceeded 75%.

Cell viability assays

Cell viability of primary human and mouse fibroblasts was evaluated using the Cell Count Kit-8 (CCK-8) according to the manufacturer's instructions. Briefly, fibroblasts were seeded into 96-well plates at a density of 8,000 cells per well in 100 μL of DMEM containing 10% FBS and 1% Penicillin-Streptomycin. After incubation for 24 h at 37°C in a humidified incubator with 5% CO_2 to allow cell attachment, LL37 peptide and siRNA were added to the culture medium for 0-24 h to assess the dose-dependent effects on cell viability. Subsequently, 10 μL of CCK-8 solution was added to each well, and the cells were incubated for an additional 2 h at 37°C. The absorbance at 450 nm was measured using a microplate reader. Each experimental condition was performed in triplicate wells, and all experiments were independently repeated at least three times. The optical density (OD) values were used to calculate the relative cell viability, expressed as a percentage of the untreated control group.

siRNA-mediated gene silencing

Gene silencing of *MRGPRX2* in primary human fibroblasts and *MRGPRB2* in primary mouse fibroblasts was achieved using small interfering RNA (siRNA)-mediated knockdown. Chemically synthesized siRNA sequences targeting *MRGPRX2* and *MRGPRB2* were purchased from OBiO Technology Co., Ltd. (Shanghai, China). The detailed sequences of siRNAs used are provided as follows. Cells were seeded into 6-well plates at approximately 50–60% confluence and transfected with 50 nM siRNA using HighGene transfection reagent following the manufacturer's recommended protocol. Briefly, siRNA and HighGene reagent were separately diluted in Opti-MEM, incubated for 5 min at room temperature, then mixed gently and incubated for 20 min to allow complex formation. The siRNA-transfection reagent complexes were then added to cells in antibiotic-free medium and incubated for 6 h. The medium was subsequently replaced with complete growth medium containing 10% FBS and 1% P/S. Cells were harvested 48–72 h post-transfection for subsequent RNA and protein analysis to evaluate knockdown efficiency.

Oligonucleotides name	Sequence (5′–3′)
MRGPRB2-mouse-si1-sense	GGAUCUAUUGGAUACUCUATT
MRGPRB2-mouse-si1-antisense	UAGAGUAUCCAAUAGAUCCTT
MRGPRB2-mouse-si2-sense	GCGGAAGACUCUCAAGCUATT
MRGPRB2-mouse-si2-antisense	UAGCUUGAGAGUCUUCCGCTT
MRGPRB2-mouse-si3-sense	GGAAGCUACUACAUCGAUATT
MRGPRB2-mouse-si3-antisense	UAUCGAUGUAGUAGCUUCCTT
MRGPRX2-human-si1-sense	GAAGGAUUCUGAUGUCUUATT
MRGPRX2-human-si1-antisense	UAAGACAUCAGAAUCCUUCTT
MRGPRX2-human-si2-sense	CGAGAAGCAGUCUGGUGUATT
MRGPRX2-human-si2-antisense	UACACCAGACUGCUUCUCGTT
MRGPRX2-human-si3-sense	CAGAAAGUACAACAGUGAATT
MRGPRX2-human-si3-antisense	UUCACUGUUGUACUUUCUGTT
Control si-sense	UUCUCCGAACGUGUCACGUTT
Control si-antisense	ACGUGACACGUUCGGAGAATT

Plasmid construction and transfection

Plasmids encoding LV-h-*MRGPRX2*-3flag and a negative control vector carrying GFP were synthesized and constructed by Hanbio Biotechnology (Shanghai, China). The target genes were subcloned into the mammalian expression vector pcDNA3.1(+) using standard molecular cloning techniques and sequence-verified to ensure accuracy.

For transient transfection, primary human HFF1 cells were seeded into 6-well plates at approximately 50–70% confluence. The plasmid DNA was diluted in Opti-MEM, and the HighGene transfection reagent was separately diluted in Opti-MEM. After 5 min of incubation at room temperature, the DNA and reagent mixtures were combined and allowed to form complexes for 20 min. The transfection complexes were then added to the cells in antibiotic-free medium and incubated for 6 h at 37°C with 5% CO_2. After incubation, the medium was replaced with complete growth medium containing 10% FBS and 1% P/S.

Transfected cells were harvested 48–72 h post-transfection for downstream analyses, including RNA extraction, protein detection, or functional assays. All plasmids underwent Sanger sequencing validation, and confirmed constructs were aliquoted and stored at −80°C for long-term preservation.

Live-cell Ca^{2+} imaging

Intracellular calcium concentration ($[Ca^{2+}]_i$) changes in primary human and mouse fibroblasts were measured using Fura-2-based ratiometric fluorescence imaging, with slight modifications. Briefly, fibroblasts were seeded onto sterile glass coverslips pre-coated with poly-L-lysine in 24-well plates and cultured overnight to allow cell attachment.

Cells were then incubated with 4 μM Fura-2 AM diluted in serum-free culture medium containing 0.02% Pluronic F-127 at 37°C for 60 min in the dark to facilitate dye loading. After loading, cells were washed three times with Hanks' Balanced Salt Solution to remove excess dye and incubated in HBSS at room temperature for an additional 30 min to allow complete de-esterification of Fura-2 AM.

Fluorescence measurements were performed using an inverted Leica fluorescence microscope equipped with 340 nm and 380 nm excitation filter wheels and a 510 nm emission filter. Time-lapse images were captured using LAS X imaging software. The ratio of fluorescence intensity at 340 nm–380 nm excitation (F340/F380) was calculated to monitor real-time changes in $[Ca^{2+}]_i$.

Baseline fluorescence ratios were recorded for each coverslip under resting conditions until stabilization. Pharmacological agents or LL37 peptides were then applied to stimulate calcium influx, and fluorescence changes were continuously monitored. The activation threshold was defined as an increase in Fura-2 ratio exceeding 3 standard deviations above the baseline, corresponding to approximately a 20% increase. Stable baseline ratios confirmed cell viability and experimental reliability. All experiments were repeated independently at least three times.

RNA extraction and RT-qPCR

Total RNA was extracted from cultured cells or tissue samples using TRIzol Reagent following the manufacturer's protocol. Briefly, cells were lysed in TRIzol and phase separation was induced by chloroform, followed by centrifugation. The aqueous phase containing RNA was collected and precipitated with isopropanol. The RNA pellet was washed with 75% ethanol, air-dried, and resuspended in RNase-free water. RNA concentration and purity were measured using a NanoDrop spectrophotometer, and integrity was assessed by agarose gel electrophoresis.

For cDNA synthesis, 1 μg of total RNA was reverse transcribed using the HyperScript III RT SuperMix for qPCR with gDNA Remover, which includes a genomic DNA removal step. The reaction was carried out according to the manufacturer's instructions.

Quantitative real-time PCR (RT-qPCR) was performed using 2 × ChamQ Universal SYBR qPCR Master Mix on a QuantStudio or CFX96 real-time PCR system. Gene-specific primers were designed to span exon-exon junctions when applicable to minimize genomic DNA amplification. The PCR cycling conditions were as follows: initial denaturation at 95°C for 30 s, followed by 40 cycles of 95°C for 10 s and 60°C for 30 s. Melt curve analysis was conducted to confirm specificity.

Relative gene expression levels were calculated using the $2^{-\Delta\Delta Ct}$ method, with GAPDH or ACTB as internal reference genes. All reactions were performed in triplicate, and no-template controls (NTCs) were included to detect potential contamination. Statistical analysis and graphing were performed using GraphPad Prism 10.0. The list of primers used is provided as follows.

Gene	Forward primer (5′-3′)	Reverse primer (5′-3′)
H-*GAPDH*	GGAGCGAGATCCCTCCAAAAT	GCTAAGCAGTTGGTGGTTGCA
M-*GAPDH*	AGGTCGGTGTGAACGGATTTG	TGTAGACCATGTAGTTGAGGTCA
H-*CAMP*	AGGTCCTCAGCTACAAGGAAG	TCTTGAAGTCACAATCCTCTGGT
H-*ACTA2*	AAAAGACAGCTACGTGGGTGA	GCCATGTTCTATCGGGTACTTC
M-*ACTA2*	CCCAGACATCAGGGAGTAATGG	TCTATCGGATACTTCAGCGTCA
H-*TGFB1*	GGCCAGATCCTGTCCAAGC	GTGGGTTTCCACCATTAGCAC
M-*TGFB1*	CTCCCGTGGCTTCTAGTGC	GCCTTAGTTTGGACAGGATCTG
H-*COL1A1*	GAGGGCCAAGACGAAGACATC	CAGATCACGTCATCGCACAAC
M-*COL1A1*	GCTCCTCTTAGGGGCCACT	CCACGTCTCACCATTGGGG
H-*COL1A2*	GTTGCTGCTTGCAGTAACCTT	AGGGCCAAGTCCAACTCCTT
M-*COL1A2*	GTAACTTCGTGCCTAGCAACA	CCTTTGTCAGAATACTGAGCAGC
H-*COL3A1*	GGAGCTGGCTACTTCTCGC	GGGAACATCCTCCTTCAACAG

(*Continued on next page*)

Continued

Gene	Forward primer (5′-3′)	Reverse primer (5′-3′)
M-*COL3A1*	CTGTAACATGGAAACTGGGGAAA	CCATAGCTGAACTGAAAACCACC
H-*FAP*	TGAACGAGTATGTTTGCAGTGG	GGTCTTTGGACAATCCCATGT
M-*FAP*	GTCACCTGATCGGCAATTTGT	CCCCATTCTGAAGGTCGTAGAT
H-*PPP3CA*	CCAAGTCACCGGCTTACAG	CCTCCTTCATAAGATGCGCCTT
M-*PPP3CA*	GTGAAAGCCGTTCCATTTCCA	GAATCGAAGCACCCTCTGTTATT
H-*NFATC1*	CACCGCATCACAGGGAAGAC	GCACAGTCAATGACGGCTC
M-*NFATC1*	GACCCGGAGTTCGACTTCG	TGACACTAGGGGACACATAACTG
H-*NFATC2*	GAGCCGAATGCACATAAGGTC	CCAGAGAGACTAGCAAGGGG
M-*NFATC2*	TCATCCAACAACAGACTGCCC	GGGAGGGAGGTCCTGAAAACT
H-*MRGPRX2*	CTGGTAGGAAACGGGTTTGTG	GCTGAGGACGTAGACAGAGAAG
M-*MRGPRX2*	ATCAAGAATCTAAGCACCTCAGC	GAAAGCAAAATCATGGCTTGGT
H-*MKI67*	GAAAGAGTGGCAACCTGCCTTC	GCACCAAGTTTTACTACATCTGCC
H-*LRRC15*	CGTTGCTGTTCCAAGCGTCCAT	GCTCAGTGGTAGAAGAGACGGA
H-*POSTN*	CAGCAAACCACCTTCACGGATC	TTAAGGAGGCGCTGAACCATGC

Western Blot

Protein expression levels in primary human and mouse fibroblasts were analyzed using Western blotting. Cells were washed twice with ice-cold PBS and lysed with ice-cold RIPA lysis buffer (pH 7.4) containing a protease and phosphatase inhibitor cocktail and 1 mmol/L PMSF. Cell lysates were incubated on ice for 30 min and centrifuged at 12,000 rpm for 15 min at 4°C to collect the supernatant.

Protein concentrations were determined using the Bicinchoninic Acid (BCA) Protein Assay Kit according to the manufacturer's instructions. Equal amounts of total protein (20–40 μg) were separated by SDS-PAGE on 8–12% polyacrylamide gels and transferred onto PVDF membranes using a semi-dry transfer system.

Membranes were blocked with 5% (w/v) Bovine Serum Albumin (BSA) dissolved in TBST (0.1% Tween 20 in TBS) for 1 h at room temperature. Subsequently, membranes were incubated overnight at 4°C with primary antibodies diluted in TBST with 5% BSA, including: CAMP, hCAP18, MrgprX2/B2, Col1a1, Col1a2, Col3a1, α-SMA, TGF-β1, Ki67, FAP, Periostin, GAPDH, and β-actin. After washing with TBST three times, membranes were incubated with horseradish peroxidase (HRP)-conjugated secondary antibodies for 2 h at room temperature.

Protein bands were visualized using enhanced chemiluminescence (ECL) detection reagent and imaged with a ChemiDoc XRS+ System. Densitometric quantification of the band intensities was performed using ImageJ software. Protein expression levels were normalized to the corresponding loading control (e.g., GAPDH or β-actin). Data were presented as fold change relative to the control group and expressed as mean ± standard error of the mean (SEM) from at least three independent experiments.

Flow cytometry

Skin single-cell suspensions were first stained with Live/Dead viability dye, followed by staining with fluorochrome-conjugated antibodies including Ly-6C, Ly-6G, CD11b, CD45R/B220, CD335, CD117, CD45, F4/80, and CD3e. Stained cells were washed, fixed using the Cytofix/Cytoperm buffer, and analyzed by a BD FACSymphony A5 Cell Analyzer with FACSDiva software. Data were processed using FlowJo (TreeStar).

RNAscope in situ hybridization

RNA *in situ* hybridization (ISH) was carried out with the RNAscope Multiplex Fluorescent Reagent Kit v2 following the manufacturer's instructions. In brief, 12-μm skin sections from mouse specimens were fixed in 4% paraformaldehyde at 4°C for 15 min, then dehydrated through a graded ethanol series (50% for 5 min, 70% for 5 min, and 100% for 5 min, repeated twice). After air-drying, sections were incubated with hydrogen peroxide at room temperature for 10 min to inhibit endogenous peroxidase activity. Antigen retrieval was achieved by boiling the slides in the target retrieval reagent for 5 min. Once cooled, the tissue was permeabilized with Protease III at 40°C for 30 min. Hybridization of probes specific to *MRGPRX2* and *MRGPRB2* mRNAs was performed at 40°C for 2 h in a HybEZ Oven. Subsequent signal amplification and fluorophore labeling followed the standard RNAscope protocol. Finally, co-localization analysis was conducted via immunofluorescence staining, as detailed in the next section.

Histology analysis

Tissue samples collected from human or mouse skin were fixed in 4% paraformaldehyde (PFA) at 4°C overnight to preserve tissue architecture. Following fixation, samples for paraffin embedding were dehydrated through a graded ethanol series (70%, 80%, 90%, 95%, and 100%) and cleared in xylene before embedding in paraffin. Paraffin-embedded tissues were sectioned at a thickness of

12 μm using a microtome. For general histological analysis, sections were stained using hematoxylin and eosin (H&E) to evaluate tissue morphology or Masson's trichrome to assess collagen deposition and fibrosis, according to standard protocols. The area of cell infiltration, dermal thickness, and collagen deposition was quantitatively analyzed using ImageJ software.

For immunofluorescent staining, fixed tissues were embedded in OCT compound (SAKURA Tissue-Tek, 4583) and frozen at −20°C. Frozen sections (12 μm) were washed with PBS and blocked with 10% Normal Donkey Serum (NDS) for 2 h at room temperature to prevent non-specific binding. Sections were then incubated overnight at 4°C in a humidified chamber with primary antibodies targeting CAMP, Keratin14, α-SMA, Collagen XVII, TGF-β1, Avidin, MPO, NFATc1, and ER-TR7. After washing with PBS, sections were incubated with appropriate fluorophore-conjugated secondary antibodies for 2 h at room temperature. Nuclei were counterstained with DAPI Fluoromount. Fluorescent images were captured using a Leica Thunder DM68 confocal microscope and analyzed using LAS X software.

RNA-seq analysis

Total RNA was extracted using TRIzol Reagent and quantified on a NanoDrop. Ribosomal RNA was removed using the Ribo-Zero Kit. The remaining RNA was fragmented in Illumina's fragmentation buffer at elevated temperature. First-strand cDNA was synthesized with random primers; the RNA template was then degraded by RNase H, and second-strand cDNA was made with DNA Pol I using dUTP. After end repair and A-tailing, Illumina adapters were ligated. USER enzyme (NEB) removed the U-containing strand to preserve directionality, and fragments of 400–500 bp were selected with AMPure XP beads. Libraries were PCR-amplified for 15 cycles with Illumina primers, purified again with AMPure XP, and assessed on a Bioanalyzer 2100 (Agilent) with the High Sensitivity DNA assay. Final libraries were sequenced (2 × 150 bp) on a NovaSeq 6000 (Illumina) by Genekinder Medicaltech (Shanghai) Co., Ltd, China.

Raw sequencing reads (FASTQ files) were subjected to quality control using fastp (0.22.0) to remove reads containing adapters, reads containing ploy-N and low-quality reads. Clean reads were mapping to the reference genome using HISAT2 v2.1.0. Gene expression levels were quantified using HTSeq (v0.9.1) and normalized as FPKM (Fragments Per Kilobase of transcript per Million mapped reads). Differentially expressed genes ($|\log2FC| > 1$, adjusted $p < 0.05$) were identified using DESeq and visualized using heatmaps generated by Pheatmap.

scRNA-seq analysis

We downloaded the dataset (GSE156326) and collected human skin and HTS cases for analysis. Cells expressing fewer than 200 or more than 5,000 detected genes, or with over 10% mitochondrial gene expression, are excluded. Data normalization and identification of highly variable genes are performed. The Seurat R package (v5.3.0) was used for normalization, scaling, and regression based on the expression table according to the UMI count of each sample. Dimensional reduction and clustering were conducted using the Seurat workflow, with batch effects corrected via Harmony (v1.2.3). Unsupervised clustering and marker gene identification were carried out using the FindAllMarkers function (logFC >0.25, min.pct >0.10) with the Wilcoxon rank-sum test.

QUANTIFICATION AND STATISTICAL ANALYSIS

All statistical analyses were performed using GraphPad Prism 10. All statistical details of experiments, including the specific statistical tests used, exact values of n, what n represents, definition of center, and dispersion and precision measures, are provided in the relevant figure legends and are summarized below. All data are presented as mean ± SEM. The exact value of n and what n represents are specified in each figure legend. For comparisons between two independent groups, two-tailed Student's *t*-tests were used. For comparisons involving three or more groups, one-way Analysis of Variance (ANOVA) with Tukey's multiple comparison post-hoc test was performed as indicated in the individual figure legends. A *p*-value of 0.05 or less was considered statistically significant, with specific thresholds denoted as: $^{*}p \leq 0.05$, $^{**}p \leq 0.01$, $^{***}p \leq 0.001$, $^{****}p \leq 0.0001$; ns indicates not significant ($p > 0.05$). Sample sizes for all experiments are indicated in the figure legends. No data were excluded from the statistical analyses other than those due to technical errors during data acquisition or processing.